5-2023

Evapotranspiration and Energy Balance of Irrigated Urban Turfgrass

Matthew D. Miksch
Utah State University

EVAPOTRANSPIRATION AND ENERGY BALANCE OF IRRIGATED URBAN TURFGRASS

by

Matthew D. Miksch

A thesis submitted in partial fulfillment
of the requirements for the degree

of

MASTER OF SCIENCE

in

Climate Science

Approved:

Lawrence E. Hipps, Ph.D. Major Professor	Shih-Yu (Simon) Wang, Ph.D. Committee Member
Alfonso Torres-Rua, Ph.D. Committee Member	D. Richard Cutler, Ph.D. Vice Provost of Graduate Studies

UTAH STATE UNIVERSITY
Logan, Utah

2023

ABSTRACT

Evapotranspiration and Energy Balance of Irrigated Urban Turfgrass

by

Matthew D. Miksch, Master of Science

Utah State University, 2023

Major Professor: Dr. Lawrence E. Hipps
Department: Plants, Soils, and Climate

Utah has the second highest per-capita domestic water usage in the United States, the majority of which is expended for outdoor irrigation. It also has a population expected to double in the next 50 years. With a majority of that growth happening in urban areas, it's important to understand how much water is being used by urban landscapes in order to plan and manage future water resources. Most current approaches to estimate evapotranspiration (ET) use the reference ET approach, which employs an empirical constant. The lack of credible measurements under various conditions results in great uncertainty for this constant. Some of our previous eddy covariance measurements have shown turfgrass ET does not conform to a unique constant value for the empirical constant.

The objectives of this thesis are to (a) use eddy covariance measurements of ET and energy balance over a suburban golf course with cool-season turfgrass to establish a data set to quantify ET and other components of energy balance and (b) use satellite imagery and a published and known remote-sensing based model to simulate the spatial distribution of evaporative fraction, or the ratio of latent heat flux (ET) to available energy, in an urban region in northern Utah.

Eddy covariance measurements of ET were collected over the 2017 and 2018 growing seasons, which translated from early- to mid-May through the end of October for this study site. Results showed that energy balance closure ranged from acceptable to good for a set of sample days, ranging anywhere from 0.69 to 0.95 with an average of 0.85. Hourly crop

coefficients and daily ET differed from the recommended crop coefficient and daily ET for cool-season turf. This difference changed throughout the growing season, indicating the need for a more dynamic approach to estimate ET for this type of urban land surface.

Remote sensing is a popular tool to estimate ET, as it provides a spatial estimate of ET that changes with landscape variability, rather than prescribing a single value to an entire area. The model known as the "triangle method" uses NDVI and brightness temperature from remote sensing imagery as inputs to determine the evaporative fraction value for each pixel. When combined with remote sensing estimates of available energy, the spatial distribution of evaporative fraction can be recovered. Both surface flux measurements and Landsat 8 satellite imagery were obtained for the growing seasons of 2017-2018 to test the approach. Results have shown the triangle method produced average evaporative fraction values comparable to observations, but there was poor fit between the model and observations. The integration of the model and its validation will provide important information about the water use of these landscapes, and the changes to be expected with varying climatic conditions.

(82 pages)

PUBLIC ABSTRACT

Evapotranspiration and Energy Balance of Irrigated Urban Turfgrass

Matthew D. Miksch

Water usage for irrigation is a big consumer of water resources in urban areas in Utah and other parts of the Intermountain Region of the Western United States. As populations continue to increase in these states, it is important to understand how much water is being used by urban landscapes in order to plan and manage future water resources. Evapotranspiration (ET), or the amount of water leaving a surface over a certain timeframe due to both transpiration from plants and evaporation from the soil, is a key variable in understanding how much water urban landscapes are really using to grow and survive. There are ways to estimate it using nearby weather station data, but this method has shown to not always be accurate for one of the more prominent urban landscapes: turfgrass. There are more rigorous ways of measuring ET, but they are much more expensive and require maintenance and processing time. Satellite remote sensing models are becoming an increasingly popular way to estimate ET as well, but they are difficult to employ in urban areas due to the dense spacing of different landscapes and man-made structures.

In this thesis, measurements of high-frequency three-dimensional wind, temperature, and humidity are collected and processed to calculate how much water was used at a golf course in a suburban area. This data is then used to validate a simple yet tested and published remote sensing model. ET measurements during the 2017 and 2018 growing season showed that in general more water was being used by the turfgrass than the recommended amount, although this changed throughout the growing season and the turfgrass was actually using less than the recommended amount during the fall months. The validation of the remote sensing model did provide a fair estimate of the average measured values, but the performance of the model was not as good as those found in other studies, likely due to properties of urban landscapes violating some of the assumptions in the model. Combining the model and its validation provide important

information on how much water urban landscapes consume, along with steps forward in modeling this water use from a remote sensing perspective.

ACKNOWLEDGMENTS

I express my gratitude towards my major professor Dr. Lawrence Hipps, along with my committee members Dr. Alfonso Torres and Dr. Simon Wang, for their assistance, guidance, and patience throughout this project.

I would like to thank the faculty, staff, and fellow graduate students both inside and outside the Plants, Soils, and Climate department for their support and encouragement. I would like to extend thanks to Jobie Carlisle, Martin Schroeder, and others at the Utah Climate Center, along with those at Apogee Instruments, Inc. and Campbell Scientific, Inc., for aiding in the instrumentation used in this project.

I would also like to thank Eagle Lake Golf Course, especially their superintendent Ronald Howard, for being accommodating while we took measurements on their property. Special thanks go to the patrons of the golf course for not hitting any of the expensive instrumentation with golf balls for the duration of the study.

I wish to thank both the iUTAH EPSCoR project (OIA - 1208732) and the United States Golf Association (USGA) for their financial support.

Finally, I want to thank my family and friends outside of the university for their words of encouragement and providing the much-needed breaks throughout my time at Utah State University.

Matthew D. Miksch

CONTENTS

LIST OF TABLES

LIST OF FIGURES

CHAPTER 1

INTRODUCTION

1.1 Background

Uncertainty in water resources is a growing concern in Utah and much of the Intermountain West in the United States. Population is expected to almost double in the next 50 years in Utah, with much of that growth being in urban areas (Perlich et al., 2017). Utah also has the second highest per capita domestic water use in the United States, using approximately 639 liters per capita per day (Dieter et al., 2018). While this accounts for only approximately 10% of the total water used in the state, it is an expensive and conspicuous use, and a majority of it is used for outdoor use during the summer months. As population increases the need for green spaces for expanding communities will also increase. Along with increased water use by population growth, water uncertainty due to climate change will also play a key role in how water is managed in the future in the Intermountain West (Barnett et al., 2008; Yoon et al., 2015).

Turfgrass is a common and popular choice for urban landscapes. It's history for recreational purposes spans far back in human history and across the globe, and before colonization the Indigenous Peoples played games on sod in the Great Plains region of North America. Modern day high-quality turfgrass use for games such as golf likely stems from the development of these types games in the lowlands of Europe, which was then brought over to the US (Roberts et al., 1992). It is often categorized into two different types: warm-season and cool-season turfgrasses. Warm-season turfgrass, such as Bahiagrass and Bermudagrass, is well suited for warmer climates and can have some drought tolerance, while cool-season turf, such as wheatgrass and Kentucky Bluegrass, thrives in cooler temperatures (18-23 °C) and can be stressed in warmer temperatures (27-35 °C). Cool season turfgrass or a combination of warm and cool season turfgrass is often used in the northern metropolitan areas of Utah in the due to it staying green longer throughout the year, even though more watering is needed during the summer. One way

to reduce water use in urban areas is to irrigate turfgrass more efficiently or provide the minimum irrigation to maintain acceptable appearance. This requires accurate monitoring of how much water is used by these landscapes.

Turfgrass is often considered an idealized surface when it comes to evapotranspiration (ET) as it is relatively uniform compared to other plant communities. Various studies have been done on ET of turfgrass with a wide variety of methods used to estimate ET (Huang and Fry, 2000; Leksungnoen et al., 2012). Despite its importance for urban water use and rather idealized surface, there is a lack of high-quality measurements of actual ET for this type of vegetation.

Most irrigation managers currently use crop coefficients (k_c) multiplied by a reference evapotranspiration value (ET_0) to estimate actual ET for turfgrass (Romero and Dukes, 2016). The reference ET value represents the ET value that would be observed for an idealized, well-watered, and green vegetated surface under the observed atmospheric conditions, assuming they would not have changed in response to that ET value. A popular use of ET_0, especially in semi-arid urban areas where landscape types are often mixed, is to use the Water Use Classification of Landscape Species, or WUCOLS (Costello and Jones, 2014), although there aren't specific recommendations for turfgrass and they default to Harivandi et al. (2009). Multiple studies have used reference ET to estimate actual ET using various coefficients for urban areas (Brown et al., 2001; Nouri et al., 2013). Soil water balance, weighing lysimeters, and chambers are also popular methods for estimating ET (Bijoor et al., 2014; Spronken-Smith et al., 2000). However, there are issues determining the accuracy of these measurements, along with what areas of surface they represent, as well as scaling them to larger surfaces. Most of these measurements are only collected at discrete points, and even in a seemingly homogeneous surface like turfgrass there can be large spatial differences in ET across the surface.

Eddy covariance is considered the best or "gold standard" approach to measure turbulent fluxes of mass and energy within the atmospheric boundary layer, including water vapor or actual ET. This is achieved through high frequency measurements of wind, temperature, and trace gases (usually water vapor and CO_2) and then using the relationships between these variables over an appropriate time period to obtain a flux.

While in principle the approach appears simple, there are many complicating factors including: siting the tower, determining the source area of the flux, finding the optimal averaging period, and performing various corrections to the raw time series data to account for complicating processes. Urban areas have further complications due to transport of energy from surrounding landscapes, which can provide additional heat sources (Feigenwinter et al., 2012; Kotthaus and Grimmond, 2012). A few studies and field campaigns have been done using eddy covariance for evapotranspiration in urban areas (Grimmond and Oke, 1999; Wang et al., 2016), but most of these studies focus on neighborhood-scale fluxes rather than individual surfaces, which doesn't provide ET values that irrigation managers can use.

While not a direct measurement of ET, remote sensing models are a powerful tool to spatially estimate ET. Different combinations of measured wavebands from earth observing satellites (e.g. MODIS, Landsat, Sentinel, WorldView) are used to estimate surface variables and properties that govern ET for a certain area. These variables are then used in models that vary greatly in complexity, ranging from simple surface radiant temperature and vegetation index-based methods (Price, 1990), to integration of vegetation index and surface temperature with land atmosphere processes (Gillies and Carlson, 1995; Petropoulos et al., 2009), to variants of this approach such as METRIC (Allen et al., 2007), and finally to more mechanistic process-based models using multiple sources of data, such as ALEXI/DisALEXI (Anderson et al., 2011). These methods allow for large-scale spatial and temporal analysis. However, these methods still require ground measurements to validate and can be difficult to implement in heterogeneous environments such as urban areas, especially in more complicated models where more processes that drive ET are considered.

1.2 Objectives

Studying ET, especially in urban areas, requires a multi-faceted approach in order to fully understand how it changes spatially. Using a combination of eddy covariance measurents and remote sensing models, this thesis gives a better understanding of how

turfgrass in an urban setting responds to varying conditions experienced in the intermountain west.

The objectives of this thesis are to (a) collect eddy covariance and energy balance measurements at an urban turfgrass site through multiple growing seasons and (b) use the observational data to validate a simple remote sensing model for this surface using imagery from the Landsat 8 platform.

CHAPTER 2

EVAPOTRANSPIRATION AND ENERGY BALANCE MEASUREMENTS OF IRRIGATED URBAN TURFGRASS

2.1 Introduction

Measuring how much water turfgrass uses in urban landscapes is a daunting task (Nouri et al., 2013). Different microclimates can exist meters apart from one another, and available nutrients can vary greatly despite best efforts. Different species of turfgrass also have different water use and optimal growing temperatures, and the type of turfgrass planted, especially in urban areas, may be selected for maintaining visual characteristics for the longest period throughout the year rather than efficient water use.

Romero and Dukes (2016) extensively review past studies on ET and crop coefficients for cool season and other turfgrass, showing the wide range of water use across turfgrass species and climates. Past studies have used a wide variety of methods to estimate ET of turfgrass, the most popular being weighing lysimeters. While these can provide relatively accurate point-measurements of ET, there are issues determining the accuracy of these measurements, along with what areas of surface they represent, as well as scaling them to larger surfaces. This is especially an issue in urban landscapes where homogeneous surfaces are a rarity.

Despite being often used for estimating ET for other landscapes, relatively few studies have used eddy covariance to estimate ET of turfgrass plots (Fenton, 2010; Jia et al., 2009). There have also been studies specifically examining ET and energy balance of urban landscapes (Grimmond and Oke, 1999; Kotthaus and Grimmond, 2012; Wang et al., 2016), but the focus is often on neighborhood-scale exchanges rather than at the plot scale. These larger-scale exchanges are very important in understanding urban energy balance and water use as a whole, but can dampen signals of specific surfaces that may be of interest for remote sensing applications and irrigation managers.

The purpose of this chapter is to (a) provide a detailed explanation of measurements made for the data used in the analysis for Chapter 3 of this thesis, (b) outline and justify any extra corrections made to the data, and (c) provide some insight into how measured ET using eddy covariance can differ compare to other popular methods of estimating ET, namely using a crop coefficient times a reference evapotranspiraiton value.

2.2 Data Processing and Methods

2.2.1 Site Description

The flux tower was located within a golf course in Roy, Utah, USA (41.15584 °N, 112.050044 °W). The golf course consists of a driving range surrounded by fairways, greens, and sand traps, with low-density deciduous trees of various species and heights (ranging from 5 - 15 m) separating the two areas. Buildings, a large parking lot, a mini-golf course, and a municipal pool line the northern edge of the golf course (Fig. 2.1). The driving range was planted with a mixture of Kentucky Bluegrass and Perennial Ryegrass kept at a height of approximately 0.05 m. Figure 2.1 shows a map of the golf course and surrounding area, along with a marker indicating where the tower was located. Winds during the growing season change diurnally due to the surrounding terrain, and are predominately from the S to SW during the afternoon hours. The golf course was automatically irrigated, usually between the hours of 0000 and 0600 MST but sometimes during the day as determined by the superintendent, using the reference ET value calculated at the weather station times an arbitrary crop coefficient.

FIG. 2.1. Map of Eagle Lake Golf Course and surrounding area, with the flux tower marked with a red "x". Sources: Esri, DigitalGlobe, GeoEye, i-cubed, USDA, USGS, AEX, Getmapping, Aerogrid, IGN, IGP, swisstopo, and the GIS User Community

2.2.2 Instrumentation

The tower was instrumented with an eddy covariance (EC) system, consisting of a CSAT-3 sonic anemometer (Campbell Scientific Inc., Logan, UT, USA) and an LI-7500 open path infra-red gas analyzer (Li-Cor Biosciences, Lincoln, NE, USA) mounted at a height of 2.78m. These instruments were sampled at a rate of 20 Hz and were oriented to the SSW to take advantage of the predominant summer afternoon wind direction. Eddy covariance measurements were only taken during the growing season (early May to late October) from 2017-2018.

Net radiation measurements were taken initially with a NR-Lite2 net radiometer (Kipp & Zonen, Delft, The Netherlands) during the 2016 and 2017 growing seasons before being replaced with SN-500 net radiometer (Apogee Instruments Inc., Logan, UT, USA) during the 2017 and 2018 growing seasons at a height of 2.06 m. Due to irrigation issues directly around the tower during part of the 2018 growing season, a second SN-500 was set up approximately 10 m to the ESE of the tower and was operated until the end of the growing

season. Soil heat flux was measured by using a combination of two Rebs soil heat flux plates (REBS, Seattle, WA, USA) buried at 0.08 m, a pair of averaging thermocouples buried at 0.02 m and 0.06 m, and a CS655 soil water content reflectometer (Campbell Scientific Inc., Logan, UT, USA) buried at 0.05 m. Surface soil heat flux was then calculated by summing the flux at the plants and the storage of energy in the soil above the heat flux plates. Both net radiation soil heat flux measurements were computed as hourly averages.

Standard meteorological measurements were also taken on the tower as part of the Utah Climate Center's Agweather network (https://climate.usu.edu/mchd/index.php). Air temperature and relative humidity were measured using a HC2S3 temperature and relative humidity probe (Rotronic Instrument Corp., Hauppauge, NY, USA) during the 2017 growing season, which was replaced by an EE08 temperature and humidity probe (E+E Elektronik, Langwiesen, Austria) at the start of the 2018 growing season. These temperature and humidity probes were installed with a TS-100 aspirated radiation shield (Apogee Instruments Inc., Logan, UT) at a height of 2 m. Rainfall was also measured but was discarded for this study due to frequent irrigation contaminating the data. Eddy covariance measurements were collected on a CR3000, and all other slow response measurements were collected on a CR1000 (Campbell Scientific Inc., Logan, UT, USA). A picture of the instrumentation is shown in Fig. 2.2. Slow response measurements were recorded as hourly averages.

FIG. 2.2. Closeup of flux tower, looking towards the ENE.

2.2.3 Eddy Covariance Data Processing

Data Pre-Processing

Preliminary data cleaning of the 20 Hz time series data is required before calculating turbulent and latent heat fluxes. The CSAT-3 and LI-7500 are prone to faulty readings when there is anything obstructing the sensor path. This can occur for a variety of reasons, ranging from insects flying in the path to irrigation/precipitation or dust. These faulty data are usually removed using statistical methods (Starkenburg et al., 2016), but these types of methods can remove data that isn't faulty which could impact the fluxes for the hour. As there currently isn't one universally accepted method to clean eddy covariance time series data, a combination of statistical and manual data cleaning techniques were used for this study.

Raw 20 Hz data was initially "cleaned" by first taking out longer (> 1 s) sections of data that had either (a) large deviations from the observed water vapor density (ρ_v) or (b)

erratic behavior in any of the 3-D wind components or sonic temperature. Days where this behavior was observed for all daytime hours were not processed. Note that for this site, irrigation (and the subsequent hard water build-up) was the most identifiable reason for removing large portions of data.

After the initial cleaning, data were then run through a Fortran program, written by the USU Biometeorology lab, that uses several window sizes that slide over the time series data to detect possible erroneous values in the measurements. For each window segment, the normalized standard deviation and deviation from the window mean is calculated for each point. The value is flagged if either of these values was outside of a set of user-defined bounds. The user then decided whether this point was an erroneous value (or a "spike") or if it was a false flag. If the data wasn't a false flag, it was removed then filled by linear interpolation between the last valid point and the next valid point. The interval for filling the data using such interpolation was restricted to periods of a few seconds. Larger intervals were removed and if they compromised a significant fraction of an hour or more, they had to be gap filled. Gaps were filled by determining the stability of evaporative fraction, $EF = LE/(Rn–G)$, for good data periods before and after the gap. The same EF values were then applied to the gap in order to recover the LE values.

Sensible and Latent Heat Flux Calculations

Turbulent latent and sensible heat fluxes were then calculated from the pre-processed data using the following equations:

$$H = \rho_a c_p \overline{w'T'} \tag{2.1}$$

$$LE = L_v \overline{w'\rho_v'} \tag{2.2}$$

where ρ_a is the density of moist air (kg m^{-3}), c_p is the specific heat of air at constant pressure (J kg^{-1} K^{-1}), L_v is the latent heat of vaporization for water (J kg^{-1}), and ρ_w is the density of water vapor. $\overline{w'T'}$ and $\overline{w'\rho_v'}$ are the deviations from the mean of vertical

wind component (w'), sonic temperature (T'), and water vapor density (ρ_v') over the time averaging period denoted by the overbar.

Various corrections were done to correct for distance between the sonic and humidity sensors, coordinate rotation, forcing the mean vertical wind to zero to account for instrument tilt errors, coordinate rotation, and density effects due to heat and water vapor transfer. First, a sliding covariance was performed to find the maximum covariance. The effects of longitudinal separation of sensors relative to the wind direction were removed by determining the covariance values as the sonic and humidity sensor data are slid forward and backwards by various values. Since any errors degrade covariance, the correct set of time series columns is the one producing the maximum covariances of heat and water vapor. Latitudinal separations relative to the wind, as well as flux loss due to path length and sensor frequency response, were corrected using relationships reported in Massman (2000). Corrections for density effects due to heat and water vapor transfer were performed following Webb et al. (1980).

Stability and Turbulence Parameters

Other micrometeorological parameters were also calculated to provide insights to characteristics of the turbulent field and atmospheric stability. The vertical flux of horizontal momentum, or τ, is defined by:

$$\tau = -\rho_a \overline{w'u'} \tag{2.3}$$

where u' (m s^{-1}) is the instantaneous deviation from the mean of horizontal wind. This value was then used to calculate the friction velocity, u_* (m s^{-1}), which is an estimate of the intensity of the turbulent field:

$$u_* = \left(\frac{\tau}{\rho_a}\right)^{1/2} = \left(\overline{u'w'}^2 + \overline{v'w'}^2\right)^{1/4} \tag{2.4}$$

where u' and v' are the instantaneous deviations of the x and y components of the wind from their mean values. The Obukhov length, which is a similarity parameter from Monin-Obukhov similarity theory, was calculated using u^* and H as follows:

$$L = \frac{-\rho_a c_p u_*^3 T}{g\kappa H} \tag{2.5}$$

where κ is the von Karman constant, which for this study was assumed equal to 0.41.

2.2.4 Energy Balance Closure

One common approach to evaluate the partitioning of net radiation or available energy, when neglecting smaller magnitude terms, is:

$$R_n = H + LE + G \tag{2.6}$$

Where R_n is the net radiation, H is the turbulent heat flux, LE is the latent heat flux, and G is the ground heat flux, all with units of W m^{-2}. When energy is conserved, the ratio of turbulent and latent heat fluxes ($H + LE$) and available energy ($R_n - G$), also known as energy balance closure, should equal one.

$$\frac{H + LE}{R_n - G} = 1 \tag{2.7}$$

However, since any errors reduce covariance values, the sum of turbulent latent and sensible heat fluxes measured by eddy covariance are usually less than the available energy, causing an energy balance closure value less than one. The lack of full energy balance closure is theorized to be caused by a variety of issues, ranging from site and canopy specific complications to methodological and instrumentation issues (Foken, 2008).

One way to combat this lack of full energy balance closure is to force closure on the turbulent latent and sensible heat fluxes by adding to each of these values. If it is assumed that although each flux is underestimated, the ratio of H and LE is accurately recovered by the calculations, then the amount added to each flux will be dependent on the Bowen ratio:

$$\beta = \frac{H}{LE} \tag{2.8}$$

Using this ratio, H and LE values were adjusted to closed values following Twine et al. (2000):

$$LE_{closed} = \frac{R_n - G}{\beta + 1} \tag{2.9}$$

$$H_{closed} = \frac{R_n - G}{1 + \frac{1}{\beta}} \tag{2.10}$$

2.2.5 Bulk Canopy Resistances

The bulk canopy resistances, written as r_a and r_s in the Penman-Monteith equation (Monteith, 1965), were calculated to see how they change with various meteorological and micrometeorological parameters outlined in previous sections.

$$\lambda ET = \frac{\Delta(R_n - G) + \rho_a c_p \frac{(e_s - e_a)}{r_a}}{\Delta + \gamma(1 + \frac{r_s}{r_a})} \tag{2.11}$$

Bulk aerodynamic resistance, or r_a, was calculated using the similarity functions based on Monin-Obukhov similarity theory as outlined in Chávez et al. (2005). First, z_{0m} and z_{0h} (m), or the roughness lengths for momentum and heat transfer, and displacement height d (m), were calculated following Brutsaert (1975, 1982) using the canopy height, h_c (m).

$$\begin{aligned} z_{0m} &= 0.123\, h_c \\ z_{0h} &= 0.1\, z_{0m} \\ d &= 0.67\, h_c \end{aligned} \tag{2.12}$$

r_a was then calculated using the following equation:

$$r_a = \frac{\ln\left(\frac{z}{z_{0m}}\right) + \Psi_h\left(\frac{z_{0h}}{L}\right) - \Psi_h\left(\frac{z}{L}\right)}{\kappa u_*} \tag{2.13}$$

where z is the measurement height above the displacement height d, and Ψ_h is the stability correction function for heat transfer. There are multiple formulations for this function, and this study uses the formulations from Foken (2008), which depend on the dimensionless stability parameter z/L.

$$\Psi_h\left(\frac{z}{L}\right) = \begin{cases} 2\ln\left(\frac{1+y}{2}\right) & \text{if } \frac{z}{L} < 0 \\ -7.8\frac{z}{L} & \text{if } \frac{z}{L} > 0 \end{cases} \tag{2.14}$$

$$y = 0.95\left[1 - 11.6\left(\frac{z}{L}\right)\right]^{1/2} \tag{2.15}$$

Under advective conditions ($H < 0$), the Monin-Obukhov length is positive, which can cause unrealistic values in r_a, since the negative H is assumed to impose stable buoyance forces to suppress turbulence. However, under advective conditions of warm and dry air from the surrounding urban areas passing over the irrigated surfaces, the physics underlying the Monin-Obukhov similarity theory are not valid, as the scales are not sufficient to result in stable effects on turbulence. So, in these cases, the formulation for r_a in neutral conditions was used:

$$r_a = \frac{\bar{u}}{u_*^2} \tag{2.16}$$

where $\bar{u}$ is the mean wind speed. Using this value of r_a, r_s was calculated using the inverted form of Equation 2.11:

$$r_s = r_a * \left(\left(\left(\frac{\Delta(R_n - G) + \rho_a c_p \frac{(e_s - e_a)}{r_a}}{\lambda ET} - \Delta\right)\gamma^{-1}\right) - 1\right) \tag{2.17}$$

2.2.6 Reference Evapotranspiration and Crop Coefficients

A popular tool used by irrigation managers is the use of reference evapotranspiration. The time and resources required to procure reliable ET measurements are oftentimes greater than the water savings for an individual plot of vegetation. Therefore, a simplification of Equation 2.11 for an idealized, well-watered surface is often employed that is able to use key variables often available from surrounding weather stations (Allen et al., 1998):

$$ET_0 = \frac{0.408\Delta\left(R_n - G\right) + \gamma\frac{900}{T+273}u_2(e_s - e_a)}{\Delta\gamma\left(1 + 0.34u_2\right)} \tag{2.18}$$

Where ET_0 is the reference evapotranspiration [mm day^{-1}], $R_n - G$ is the available energy [MJ m^{-2} day^{-1}], u_2 is the wind speed at 2 m above the surface [m s^{-1}], $e_s - e_a$ is the saturation vapor pressure deficit [kPa], Δ is the slope of the vapor pressure curve [kPa °C^{-1}], and γ is the psychrometric constant [kPa °C^{-1}]. $R_n - G$ is usually not available from standard weather stations, so it is often parameterized using the formulations listed in Allen et al. (1998).

ET_0 has been found to overestimate ET for some surfaces due to the idealized surface not representing all crops and vegetation. Therefore, an empirically derived "crop coefficient" (K_c) is used to modify ET_0 so that it can be used to estimate water use for irrigation and water balance studies:

$$K_c = \frac{ET_a}{ET_0} \tag{2.19}$$

where ET_a is the actual evapotranspiration. K_c can be calculated at an hourly, daily, or monthly timescale depending on the application. The recommended crop coefficent for cool-season turfgrasses, such as Kentucky Bluegrass or Perrenial Ryegrass, is 0.8 for optimal irrigation or 0.6 for deficit irrigation (Harivandi et al., 2009).

2.3 Results and Discussion

2.3.1 Spectral Analysis for Choice of Valid Wind Directions

When initially deciding where the flux tower would be installed on the golf course, one of the main constraints was making sure the predominant summertime afternoon wind direction was obstruction-free while not being in the way of golf course operations. The solution was to put the tower in an out-of-bounds area between the fairways and the driving range. Subsequently this caused another issue where the southerly and southeasterly fetches had low-density tree plantings and reduced fetch of turfgrass. It was decided early on that the northerly and southerly sectors, shown as red in Fig. 2.3, would not be used in the verification in Chapter 3 due to buildings, parking lots, and a small pond to the north and tall trees directly south of the site. However, the built suburban areas to the east and southeast (shaded orange in Fig. 2.3) were $>$ 100 m away from the station and only a few

trees around the main fairway, and it was unclear if these trees would have an effect on the turbulent fluxes.

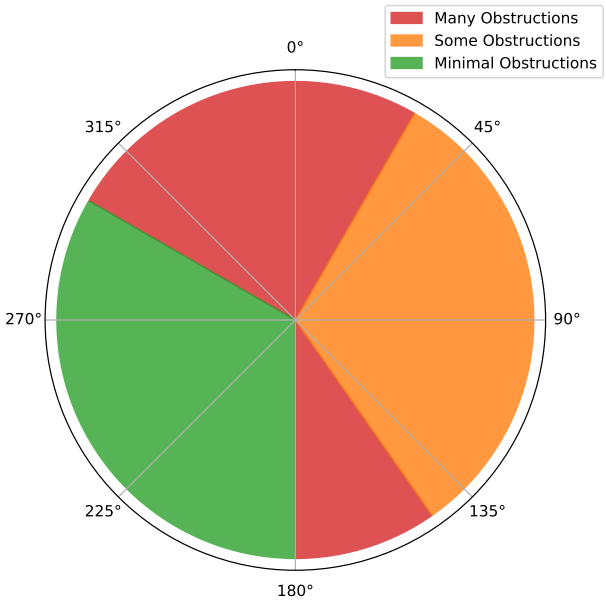

FIG. 2.3. Diagram showing the approximate directions relative to the tower of large obstructions (e.g. pools, parking lots, trees) in red, reduced turfgrass fetch or low-density tree plantings in orange, and ideal fetch in green.

To examine whether these sparsely spaced trees had an effect on the latent heat fluxes, power cospectra were calculated for a few select hours. Since most of the ET occurred during the afternoon, it was decided that only hours that met the following criteria would be used: (a) between the hours of 1200 - 1600 MST, (b) wind speed < 2 m s^{-1} to match typical summertime conditions, and (c) wind directions between approximately 30° and 145°. Due to the diurnal nature of wind at this site during the summer months, only a few individual hours met these criteria, and they are compared against two hours that occurred during southwest winds in Fig. 2.4.

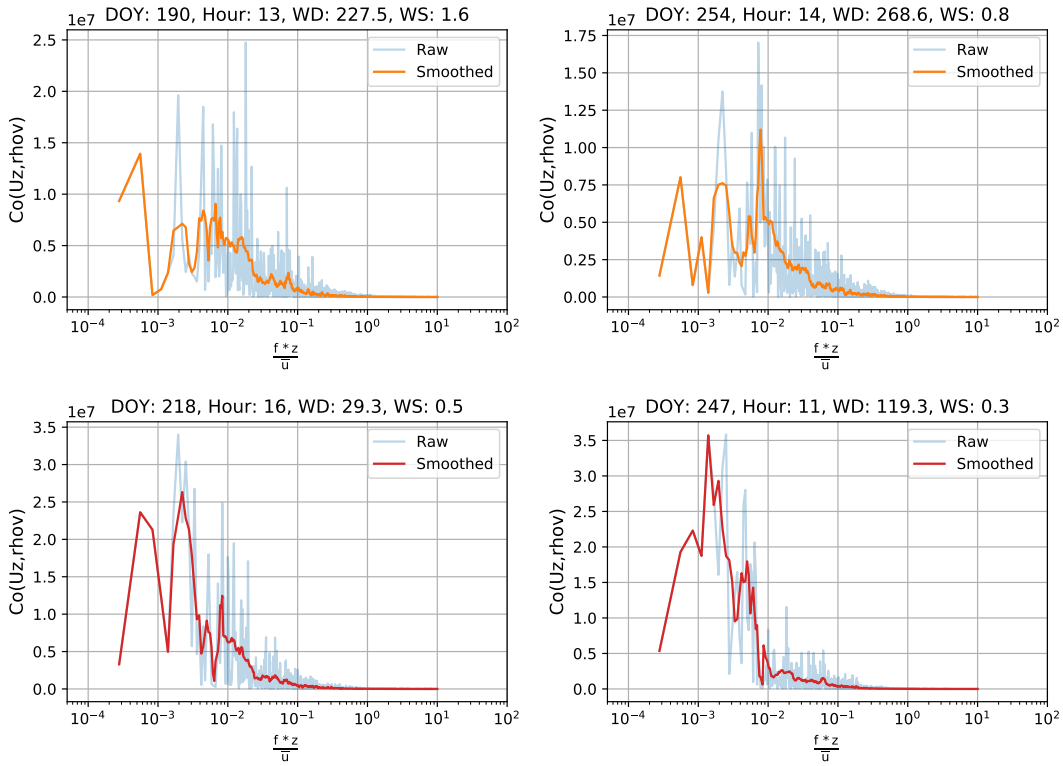

FIG. 2.4. Cospectra for sample hours during the 2018 growing season. (top) Sample hours with good fetch. (bottom) sample hours with fetch between approximately 30° and 145°. The x-axes are normalized by $\frac{z}{\overline{u}}$.

These spectra were calculated using the variables w and ρ_v for the period of one hour, or 72,000 observations taken at 20 Hz. The data were then detrended and a Hanning window was applied to minimize spectral leakage. Fast Fourier transforms (FFTs) were then performed to obtain the power spectra for each variable and the cospectra for the pair of variables. The frequencies for these spectra cospectra were then normalized by multiplying the frequencies by the measurement height and dividing by the mean horizontal wind speed for the hour.

The sample cospectra in Fig. 2.4 indicate that there was a shift in the highest contributing frequencies with the two differing wind directions. When the direction was from the northeast to southeast (red lines), the frequencies that contributed the most to the power spectrum were lower and more defined than when the wind direction was from the southwest (orange lines). This shift in frequencies suggests that there is a change in the turbulent field when the wind direction is from the northeast to southeast, and could

possibly have an effect on the latent heat fluxes. For this reason, along with the possibility that the shift towards lower frequencies could mean that the hourly averaging period may not be adequate for these wind directions, hours with these wind directions were not used for the analysis in Chapter 3 of this thesis.

2.3.2 Energy Balance Closure

Choice of Valid Wind Directions

Energy balance closure, earlier defined by Equation 2.7, is not fully reached at many sites across a wide variety of ecosystems due to many factors, ranging from significant unmeasured storage terms to large, mesoscale eddies that can be missed by eddy covariance measurements (Foken, 2008). To better understand how energy balance closure changes with ideal vs. not-ideal fetch at this site, hourly closure values were calculated for all hours during the 2017 and 2018 growing season.

Figure 2.5 shows the distribution of hourly closure values when the fetch was ideal (in blue), as well as when the fetch was not ideal (shown in red). Median hourly closure values were typically higher when the wind was from 180° - 300° than from the other directions, which support the assertion that obstructions weakened the covariance and lower the fluxes, causing lower closure values.

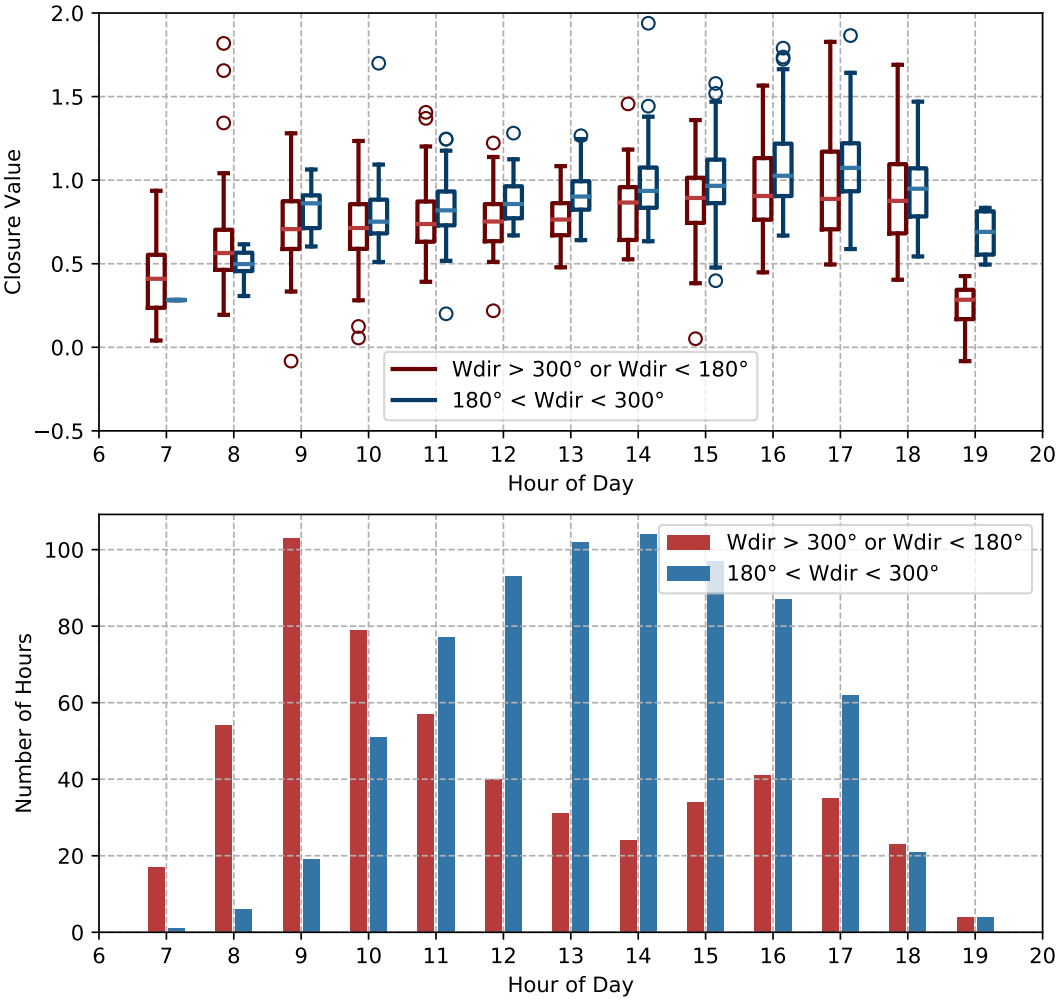

FIG. 2.5. Top: box-and-whisker plots of hourly closure values for southwest fetch (blue) and all other wind directions (red), with outliers shown as circles. Bottom: number of hours for each box-and-whisker plots, with the colors corresponding to the fetches described in the above plot.

Daily Energy Balance

Hourly closure values are often not the best measure of energy balance closure due to the mismatch between the timescales that the different components of energy balance occur. Soil heat flux has a variable thermal lag, and is not in phase with the other "fast" components of the energy balance. Such incommensurate timescales can cause closure to vary during the daytime hours, increasing as shown in Fig. 2.5.

To get around the issue, daily closure values are a more realistic way to quantify energy balance closure. Daily closures are not simply an average of all the hourly closure values

during the daytime. Instead, each component of closure is summed up for the day and then closure is calculated with these values. In this way, the periods with large fluxes receive the appropriate larger weight. Some sample daily closure values are shown in Table 2.1. These closure values are typical for eddy covariance systems, ranging from 0.69 to 0.95, and averaged about 0.85 for the days shown. Due to the lack of closure on certain days, it was decided that closure would be forced on the latent and sensible heat fluxes using Equations 2.9 and 2.10.

TABLE. 2.1. Daily closure values for two stretches of days during the 2018 growing season. The number of hours indicates how many hours during the day ($R_n > 50$) were used that also had good fetch according to Fig. 2.3.

Day of Year	**Daily Closure**	**Number of Hours**
169	0.79	11
170	0.88	10
171	0.76	10
172	0.69	11
173	0.81	7
224	0.95	6
225	0.91	6
226	0.93	9
227	0.91	8
228	0.82	8

These closure values were comparable to those found for other stations located in a wide variety of ecosystems (Wilson et al., 2002). Not shown here were days without an adequate number of hours with proper fetch, which frequently occurred during the morning hours in the summer months due to diurnal changes in wind direction arising from the surrounding terrain. This caused a large bias towards afternoon hourly closure values, which were often higher than the daily closure values due to the time lag issue between the ground heat flux and the other measured components of energy balance. Still, there were no obvious reasons to discount the measurements from the eddy covariance system.

2.3.3 Bulk Canopy Resistances

Bulk canopy resistances (r_a and r_s) play a significant role in modeling ET in the

Penman-Monteith equation (Monteith, 1965). Bulk aerodynamic resistance (r_a) values had a mean value of 73.24 s m^{-1} and a standard deviation of 35.60 s m^{-1}. Stomatal resistance (r_s) was on average higher than r_a, with a mean value of 154.86 s m^{-1} and a standard deviation of 129.47 s m^{-1}, which is higher than the resistance used for the reference crop in the reference crop ($r_s = 70$ s m^{-1}). The large standard deviation is likely due to outliers when solving the inverse Penman-Monteith equation (Equation 2.17) and the tendency for r_s to increase throughout the day.

When dealing with bulk resistance parameters, it is useful to look at bulk resistance for sample days at hourly time steps rather than only the overarching statistics in order to understand their trends on hourly timescales. Figure 2.6 shows a sample day with bulk resistances on the top plot and the components of energy balance on the bottom, with measured vapor pressure deficit also plotted on both subplots. r_a showed a general decreasing trend, while r_s decreased until around mid-day, then started increasing, especially near the end of the day. The increase in r_s coincided with decreases in LE, and followed increased saturation deficit, as might be expected for turfgrass (Fenton, 2010). Kentucky bluegrass can be stressed at temperatures above 27° C, and air temperatures during the afternoon hours are frequently above this threshold at the study site.

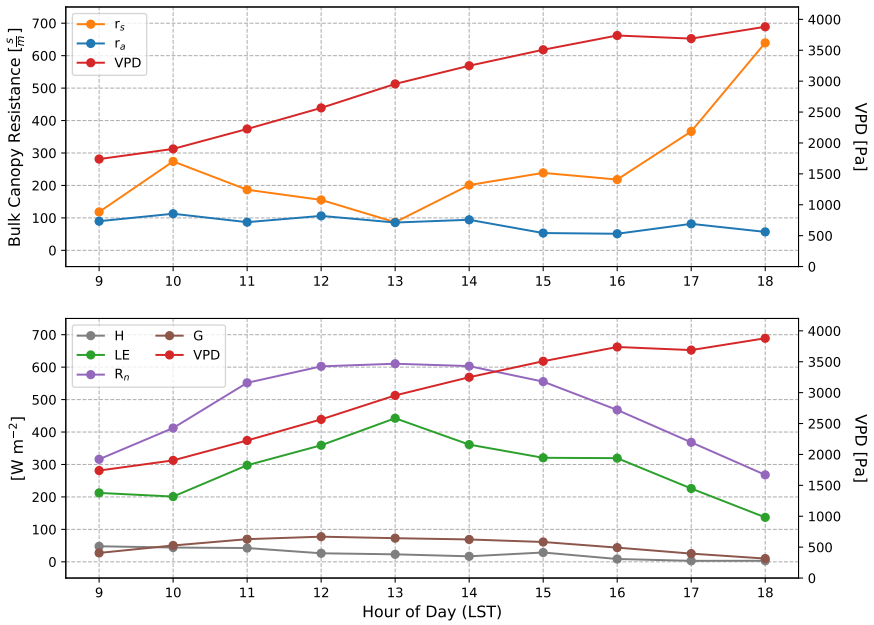

FIG. 2.6. (top) Bulk canopy resistances and (bottom) components of energy balance during the day of June 27th, 2018, with both plots also showing vapor pressure deficit.

2.3.4 Daily ET

Hourly Crop Coefficients (K_c)

As mentioned earlier in the results section, parts of the eddy covariance dataset were discarded due to suboptimal fetches to the south and east of the flux tower. Normally the preferred method of gap filling discarded hours is calculating the stability of the evaporative fraction for surrounding hours, then filling the missing hour with that fraction times available energy. However, many of the missing hours occurred during the morning before the winds switched to a direction with optimal fetch, meaning that evaluating the stability of evaporative fraction was frequently not possible.

Instead, high-quality hourly crop coefficients were empirically derived for all valid hours of the dataset using reference evapotranspiration calculated using data from the weather station co-inhabiting the flux tower. This was initially performed at monthly intervals during the growing season to see if there were any seasonal changes in the hourly crop coefficients. It was found that the hourly crop coefficients fell into two distinct categories: late spring into late summer (months 5-8) and fall (months 9-10), both shown in Fig. 2.7 for closed and unclosed latent heat fluxes.

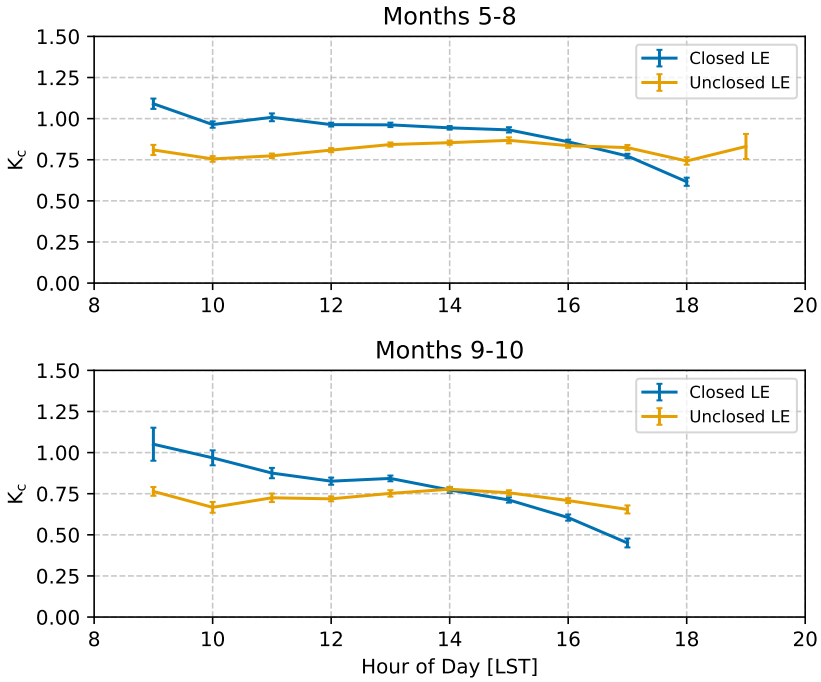

FIG. 2.7. Mean hourly K_c values calculated from both closed and unclosed measured latent heat fluxes, with bars indicating the standard error of the mean. Hours that had >10% standard error of the mean are excluded.

Decent approximations were able to be made for most of the daytime hours, although large standard errors of the means during the early morning and late evening hours resulted in those values being discarded. In those cases, the missing hours were interpolated to the mean daytime value, which usually followed the same trend as the values that were discarded due to high error values, and reference ET values were relatively low during those periods regardless. Nighttime eddy covariance values were rarely used as the turbulent intensity was usually not high enough and irrigation caused erroneous measurements during the late night and early morning hours, but nighttime ET was considered to be negligible for this type of surface.

Summer average hourly K_c values using closed latent heat values tended to decrease throughout the day, and were similar to the hourly values for the non-advective day in Fenton (2010), despite both advective and non-advective days counting towards these averages. It is possible that the bulk stomatal resistance generally decreased throughout the day, such as in Fig. 2.6. Forcing closure also seems to play a role in this decreasing

trend, as unclosed hourly K_c values tended to stay fairly consistent throughout the day.

The largest difference between summer and fall hourly K_c values was after approximately 1000 MST for the values derived from the closed LE values. During the summer, hourly K_c values were close to 1.0 before decreasing in the late afternoon. On the other hand, Fall K_c values decreased during most of the day, ending at just below 0.5 by the late afternoon. It is unsure why the decrease is linear in the Fall and non-linear during the late Spring and Summer months, although the explanation may not be purely physical given how the reference ET equation is highly parameterized.

Daily ET During 2017 and 2018 Growing Seasons

Daily ET values varied throughout the growing season during both 2017 and 2018, and not one estimation (closed LE, unclosed LE, or reference ET times a crop coefficient of 0.8) was higher than the others for the entire growing season. Daily ET increased until June and early July, where high ET days ranged from 6 - 8 mm day^{-1}. After this initial peak values ranged from 3 - 6 mm day^{-1}, until tailing off to 1 - 3 mm day^{-1} by October. Daily ET values were similar to what was reported in Fenton (2010), but the pattern in daily ET has more of a peaked appearance compared to a curve. This could possibly be due to both 2017 and 2018 being a particularly dry and warm summers, and some of the turf was starting to show signs of stress later in the summer even though the course was regularly irrigated until the end of the growing season.

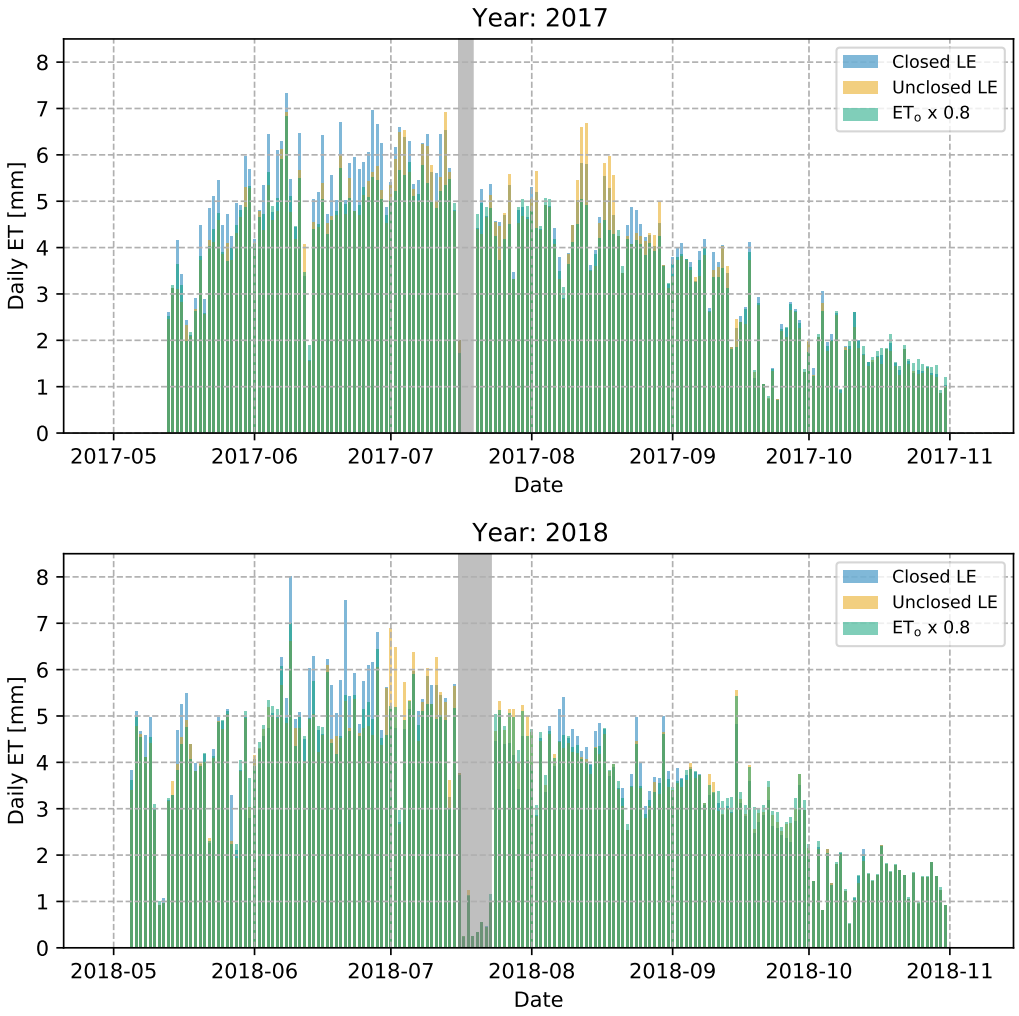

FIG. 2.8. Daily ET values using gapfilled data, with missing hours filled with a crop coefficient (found in Fig. 2.7) times reference evapotranspiration. Dates with instrument outages are shaded in gray.

Not one approach in Fig. 2.8 is consistently higher than the others throughout the entire growing season. Daily ET estimates using closed LE tend to produce higher values during the early-summer, but by the mid- to late-summer both closed and unclosed LE values produce higher values than the reference ET estimation. Usually forcing closure increases LE estimates and therefore daily ET, but highly advective conditions often seen in green spaces in urban areas may have played a role in the overall reduction of daily ET on these particular dates. Later in the season reference values tend to produce the highest estimate of daily ET, although the water use is much lower at that point in the season. In

this part of the Intermountain West, precipitation events start to become more frequent as well, reducing the need for irrigation.

The daily ET values are, on average, slightly lower than those found in other studies in the literature that measured ET of Kentucky Bluegrass. Feldhake et al. (1983) found that Kentucky Bluegrass daily ET ranged from 4.69 mm day^{-1} to 6.30 mm day^{-1} using weighing lysimeters with various treatments for a semi-shaded urban plot in Fort Collins, CO. In comparison the golf course had an average of 4.89 mm day^{-1} in 2017 during the peak summertime months. Perennial Ryegrass typically has lower water consumption (only 76% in Green et al. (1990) for the lowest transpiring Kentucky Bluegrass cultivar under optimized conditions, but 107% in Aronson et al. (1987)), which may partially explain the lower ET values at the golf course. Also, the study goals of Feldhake et al. (1983) were more focused on examining differences between treatments rather than measuring one specific surface over a large area.

Over the entire season daily ET estimates using closed LE values were greater than both unclosed LE and reference ET with a K_c of 0.8. Seasonal ET totals in 2017 were: 662.7, 626.4, and 611.9 mm for closed LE, unclosed LE, and reference ET with a K_c of 0.8, respectively. Despite a longer measurement period seasonal ET totals in 2018 were slightly lower than 2017: 649.3, 632.1, and 635.8 for closed LE, unclosed LE, and reference ET with a K_c of 0.8, respectively. While these seasonal values, especially in 2018, are fairly similar to each other, the aforementioned differences throughout the season likely lead to some of the visual quality decreases seen at the golf course by the late summer.

2.4 Conclusions

Eddy covariance measurements of an urban landscape consisting of irrigated cool-season turfgrass in a semi-arid region were collected during the 2017 and 2018 growing seasons, and were found to be generally high quality with an average energy balance closure of 0.85 during a stretch of selected sample dates.

There were caveats to using parts of the dataset. Morning measurements were often questionable, due to fetch not being ideal for a long enough distance upwind of the tower. Spectral analysis of sample hours showed that there was a shift in the cospectra towards

lower frequencies, indicating that there may be changes to the turbulent field or inadequate averaging times when the tower footprint was located in non-ideal fetch. Hourly closure values were also lower when the hourly averaged wind direction was from a direction with non-idealized fetch. However, the bulk of mid-day and afternoon measurements had adequate fetch, which was when most of the ET occurred.

Of note the average bulk stomatal resistance from this study seems to be much higher than the single value used in the reference evapotranspiration equation (154.9 s m^{-1} vs. 70 s^{-1}) and is dynamic rather than static, with values increasing (sometimes drastically) throughout the day.

Many other studies have found that turfgrass, located in an urban landscape or otherwise, differ from the recommended crop coefficients, and results from this study concur with those findings on an hourly timescale (Fenton, 2010; Romero and Dukes, 2016). When using LE values that were not subject to energy balance closure (unclosed), hourly K_c values were fairly close to the recommended K_c value of 0.8. Forcing closure increased the hourly K_c values to be higher during the morning and mid-day hours, but they decreased as the day went on, with a non-linear trend during the summer months and a more linear trend during the fall. If this type of method is going to be used for gapfilling sites that face similar fetch issues, physical explanations need to be developed as to why these types of decreases change during different parts of the season.

Despite these interesting hourly differences, irrigation of these landscapes are performed at daily or even weekly intervals. Gapfilling of the low-quality hours lead to daily ET values that were comparable on a seasonal scale to the recommended K_c value of 0.8 times reference ET. However, the recommended ET values tended to underestimate the actual ET, sometimes up to 1-2 mm day^{-1}, and overestimated during the fall months, leading to a deficit when precipitation is likely to occur in this portion of the Western US. Therefore, more robust daily K_c values are recommended to be developed for this and other large urban and suburban landscapes that may not adhere to the recommended ET values derived from reference evapotranspiration.

Collecting high-quality ET datasets is just one part in understanding the urban water and energy balance. As shown here even the most "ideal" urban landscapes may not adhere

to expected values at finer or longer timescales. Data that were not used in this study, such as hours without ideal fetch, may be useful in understanding advection processes from surrounding urban areas.

CHAPTER 3

USING THE "TRIANGLE METHOD" TO ESTIMATE EVAPORATIVE FRACTION OF IRRIGATED URBAN TURFGRASS

3.1 Introduction

Remote sensing of land surface processes in urban areas is difficult logistically and therefore has not been employed nearly as much as other surface types. High land surface heterogeneity in urban surfaces relative to the often coarser pixel resolution of satellite platforms makes it challenging to decipher what is happening at the surface for each land use type within the pixel. Also, surfaces such as parking lots and roofs have different thermal and optical properties compared to natural surfaces such as soil and vegetation. Finally, vegetation type within each pixel is often mixed, even in open green spaces such as parks and golf courses.

Still, there is a need for active monitoring of land surface processes within urban landscapes, especially for evapotranspiration (ET) in water limited areas. One of these places is the Intermountain Region of the Western United States, where states such as Utah are expected to double in population (Perlich et al., 2017) and high amounts of domestic water use, most of which goes to irrigation (Dieter et al., 2018). Along with increased water use by population growth, water uncertainty due to climate change will also play a key role in how water is managed in the future in the Intermountain West (Barnett et al., 2008; Yoon et al., 2015).

While not a direct measurement of ET, remote sensing models are a powerful tool to spatially estimate ET. Different combinations of measured wavebands from earth observing satellites (e.g. MODIS, Landsat, Sentinel, WorldView) are used to estimate surface variables and properties that govern ET for a certain area. These variables are then used in models that vary greatly in complexity, ranging from simple surface radiant temperature and vegetation index-based methods (Price, 1990), to integration of vegetation index and surface temperature with land atmosphere processes (Gillies and

Carlson, 1995; Petropoulos et al., 2009), to variants of this approach such as METRIC (Allen et al., 2007), and finally to more mechanistic process-based models using multiple sources of data, such as ALEXI/DisALEXI (Anderson et al., 2011). These methods allow for large-scale spatial and temporal analysis. However, these methods still require ground measurements to validate, and can be difficult to implement in heterogeneous environments such as urban areas, especially in more complicated models where more processes that drive ET are considered.

There have been some attempts to quantify ET of urban landscapes with remote sensing models, using methods ranging from empirical relationships between neighborhood-scale ET measurements and satellite products (Wang et al., 2016) to correlating water delivery data and other parameters to vegetation indices (Johnson and Belitz, 2012).

A very common landscape vegetation in urban regions is irrigated turfgrass. Although most of it is "cool season" species, it is very common in the arid Intermountain West due to it's visual qualities throughout the growing season. In order to address the role of irrigated turfgrass in water resources, reliable values of turfgrass ET and its spacial distribution need to be determined. Here, we address two issues with the following objectives:

1. quantifying the ET of turfgrass with eddy covariance, the gold standard methodology, and using the results to validate a published remote sensing model, and

2. examining the special challenges posed by heterogeneous urban surfaces for adapting remote sensing ET models.

In an attempt to better characterize how urban land covers impact remote sensing models, we made eddy covariance ET measurements at a golf course in an urban area to validate a simple remote sensing model called the "triangle method" for this particular surface using imagery from the Landsat 8 platform.

3.2 The Triangle Method

The "triangle method" is based on the relationship between surface temperature (T_s) and normalized difference vegetation indices (NDVI). This relationship was first explored by Price (1990) as a way to estimate surface fluxes without ancillary atmospheric and surface

measurements. This method uses surface radiant temperature and vegetation indices to establish boundaries used in surface energy balance models. This was expanded on by (Gillies and Carlson, 1995; Jiang and Islam, 2001; Petropoulos et al., 2009), and is now used in varying capacities in more modern remote sensing models. The approach in this study follows the later geometric approach to the method described in Carlson (2007) and Carlson (2013). The normalized difference vegetation index, or NDVI, is a measure of greenness of a pixel due to vegetation and is one of the most popular vegetation indices due to its relationship to important ground parameters such as leaf area index and fractional cover. It is defined as:

$$NDVI = \frac{NIR - Red}{NIR + Red} \tag{3.1}$$

where NIR is the "near infrared" waveband (0.85 - 0.88 μm on Landsat 8) and Red is the red waveband (0.64 - 0.67 μm on Landsat 8). One distinct advantage of using the geometric method from Carlson (2013) is the lack of need for complicated soil-vegetation-atmosphere transfer (SVAT) models and for corrections to get land surface temperature. Brightness temperature and NDVI were normalized using the following equations (Carlson and Ripley, 1997):

$$T^* = \frac{T_{ir} - T_{min}}{T_{max} - T_{min}} \tag{3.2}$$

$$Fr = \left(\frac{NDVI - NDVI_o}{NDVI_s - NDVI_o} \right)^2 \tag{3.3}$$

where T_{ir} is the brightness temperature for each pixel, T_{min} and T_{max} are the minimum and maximum brightness temperatures for the domain, $NDVI$ is the NDVI for each pixel, and $NDVI_o$ and $NDVI_s$ are the minimum and maximum NDVI values for the triangle. Fr represents the fractional vegetation cover.

Once the variables are normalized, and a wide enough variety of land surfaces are included, a triangle or trapezoidal shape forms in the T_s-VI space, as shown by the sample plot in Fig. 3.1. Constrains imposed by the energy balance can be inferred by quantifying

the left and right edges of the triangle. The left edge of the triangle is considered the "cold edge", or the line of maximum soil wetness, and is a constant value for all fractional covers with $T^* = 0$. The right edge of the triangle, or the "warm edge", is the zero isopleth for soil evaporation. The placement of this warm edge is more arbitrary than the cold edge, although some attempts have been made to automate the placement (Tang et al., 2010). A sample triangle with the aforementioned variables and attributes are shown in Fig. 3.1.

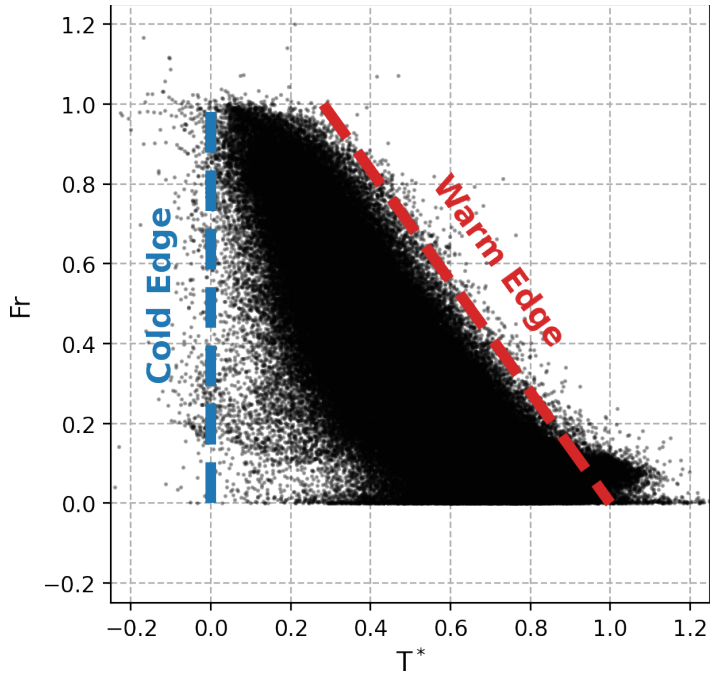

FIG. 3.1. A sample date (2016-07-03) showing the normalized T$_i r$-VI space, corresponding to T* and Fr, respectively. The cold and warm edges are displayed using blue and red dashed lines.

Once the triangle is normalized and the cold and warm edges determined, evaporative fraction (EF), defined by ET divided by available energy, can be calculated by using the following equations:

$$EF_{soil} = 1 - \frac{T^*_{pixel}}{T^*_{we}} \tag{3.4}$$

$$EF_{veg} = 1.0 \tag{3.5}$$

$$EF_{tot} = EF_{soil}(1 - Fr) + EF_{veg} \times Fr \tag{3.6}$$

where T^*_{pixel} is T^* for each individual pixel, and T^*_{we} is T^* at the warm edge for the same value of Fr. Evaporative fraction is defined as:

$$EF = \frac{LE}{R_n - G} \tag{3.7}$$

where LE is the latent heat flux (W m^{-2}), R_n is the net radiation (W m^{-2}), and G is the ground heat flux (W m^{-2}). R_n and G can be modeled using approaches such as Jiang and Islam (2001), but for this study R_n and G values from the observed data were used to avoid uncertainties introduced by modeling these values. Essentially, the above approach quantifies the EF value of any pixel in terms of the relative distance between the warm and cold edges of the triangle.

3.3 Methods

3.3.1 Study Area

The area of interest is a subsection of the northern Wasatch Front located in Utah, USA (Fig. 3.2). The Wasatch Front is a 120 mile long sprawling metropolitan region oriented north-south along the Wasatch Range, and it includes approximately 80% of the state's population. This subsection includes most of the Ogden-Clearfield metropolitan area, and is characterized by a mixture of low- and medium-density urban areas, industrial parks, two airports (one being a large air force base), and irrigated agriculture along most of the western edge.

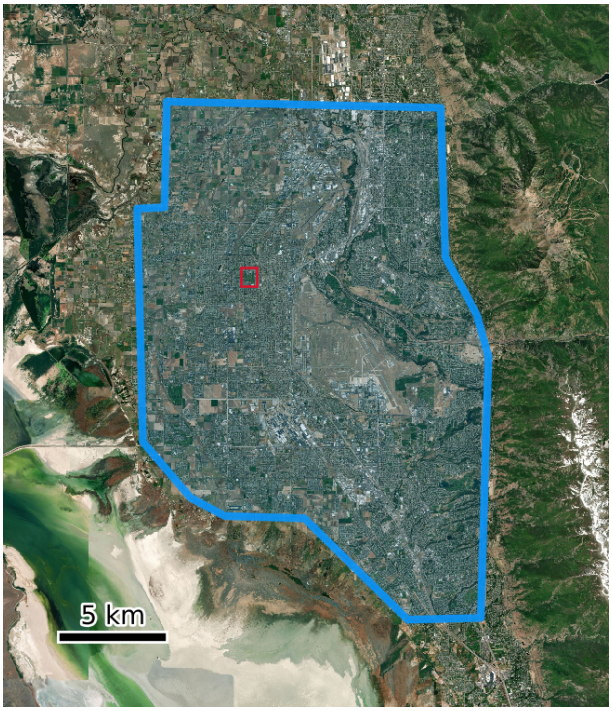

FIG. 3.2. Study area, with urban area outlined and shaded in blue. The Eagle Lake Golf Course is outlined in red, shown in Fig. 3.3. Sources: Esri, DigitalGlobe, GeoEye, i-cubed, USDA, USGS, AEX, Getmapping, Aerogrid, IGN, IGP, swisstopo, and the GIS User Community

3.3.2 Ground Observations

The eddy covariance flux tower was located within a golf course in Roy, Utah, USA (41.15584 °N, 112.050044 °W). The golf course consists of a driving range surrounded by fairways, greens, and sand traps, with a rather low density of deciduous trees of various species and heights (ranging from 5 - 15 m) separating the two areas. Buildings, a large parking lot, a mini-golf course, and a municipal pool lined the northern edge of the golf course (Fig. 3.3). The driving range and fairways are planted with a mixture of Kentucky Bluegrass and perennial ryegrass kept at a height of approximately 0.05 m. Figure 3.3 shows a map of the golf course and surrounding area, along with a marker indicating where the tower was located. Winds during the growing season are predominately from the S to SW. The golf course was automatically irrigated, usually between the hours of 0000 and 0600 MST, on a schedule set by the manger using the reference ET value calculated at the weather station times an arbitrary crop coefficient.

FIG. 3.3. Map of Eagle Lake Golf Course and surrounding area, with the flux tower marked with a red "x". Sources: Esri, DigitalGlobe, GeoEye, i-cubed, USDA, USGS, AEX, Getmapping, Aerogrid, IGN, IGP, swisstopo, and the GIS User Community

The eddy covariance tower is shown in Fig. 3.4. The turbulence sensors consisted of a 3-dimensional sonic anemometer (Model CSAT3; Campbell Scientific Inc., USA), and a fast response water vapor and CO2 sensor (Model LI-7500; LiCor Inc., USA). These sensors were mounted at a height of 2.78 m, and sampled at 20 Hz with a CR3000 data logger (Campbell Scientific Inc.) Net radiation was measured using a four way net radiometer (Apogee Instruments, Logan, UT) mounted at 2 m above the surface.

In order to compute the turbulence fluxes of sensible and latent heat, a series of analyses must be performed on the 20 Hz time series data. This includes: removing spikes and sections of bad data; coordinate rotation to remove errors due to the non-zero tilt of the sonic anemometer; corrections for frequency response and path length of the sensors; adjusting for the spatial separation of the sonic anemometer and water vapor sensor, and correcting for the effect of water vapor density on the fluxes (Massman, 2000; Webb et al., 1980). When proper analyses and corrections are implemented, the turbulent fluxes of both sensible and latent heat can be calculated. Performing cross spectral analyses allows verification the

correct time averaging period, which is generally on the order of hourly. The above analyses were conducted using Fortran code written and tested at the USU Biometeorology lab.

The soil heat flux was estimated using soil heat flux plates (REBS Inc., USA) buried at a depth of 0,08 m, with averaging thermocouples placed in the layer of soil between the surface and 0.08m. A soil moisture measurement (Model CS 650, Campbell Scientific) was also made in the same 0.08 m layer. The surface soil heat flux was then calculated as the sum of the flux at the plate plus the energy stored in the layer above. When the sensible and latent heat fluxes were combined with the net radiation and soil heat flux results, the entire surface energy balance was quantified.

Hourly latent and sensible heat fluxes were then calculated for the 2017 and 2018 growing seasons (from early May until late October). In order to compare hourly values against instantaneous images from the remote sensing platforms, linear interpolation was used between hourly averages to get "instantaneous" values for each satellite overpass time.

FIG. 3.4. Picture of the flux tower looking to the southwest

3.3.3 Remote Sensing Data

All products other than Landsat 8 surface reflectance bands for the thermal sharpening algorithm were pre-processed and downloaded using Google Earth Engine (GEE). This is

an online platform that allows users to access, process, and do calculations on various gridded datasets hosted on Google's servers. In order to access these data, users must run scripts written using Javascript (which is the most common approach when running on GEE's interactive coding page) or Python (which doesn't offer the interactivity of GEE's interactive coding page but is much more flexible for server applications) utilizing GEE's API.

The product used for this study was the Landsat 8 Surface Reflectance product. This product is a level-2 product, which uses the Landsat 8 Surface Reflectance Code (LaSRC) algorithm to correct top of atmosphere (TOA) reflectance bands for atmospheric effects. This product also includes TOA Brightness Temperature for the thermal bands.

Landsat 8 Surface Reflectance bands used in the thermal sharpening algorithm mentioned in the next section were downloaded using the EROS Science Processing Architecture (ESPA) bulk ordering tool. The surface reflectance bands and TOA brightness temperature used for this study were subset and downloaded to a local machine using GEE.

Landsat 8 Thermal Bands

Unfortunately, the thermal bands provided by GEE were interpolated to 30 m using bicubic convolution, which is not ideal for areas with high surface temperature heterogeneity like urban landscapes. These data were still used for calculating evaporative fraction, but multiple thermal band sharpening algorithms are available in the literature (Bonafoni et al., 2016; Gao et al., 2012), which use the higher resolution optical bands to better estimate the thermal bands at higher resolutions. These algorithms are used to better capture the surface heterogeneity of surface temperatures.

For this study the approach of Gao et al. (2012) was used to sharpen the thermal bands. This method utilizes all of the shortwave bands (resolution 30 m) to find spatial patterns using a data mining approach. The default window size of 200 pixels was used for the local model, which resulted in much sharper thermal bands with occasional noise in areas with high surface heterogeneity (Fig. 3.5). Clearly, the procedure of Gao et al. (2012) results in far superior images than the default bicubic convolution. The noise could possibly be

reduced further by decreasing the default window size, but without high resolution airborne or UAV thermal measurements to verify the algorithm in this landscape, it was decided that window size testing was beyond the scope of this study. The thermal sharpening used here was deemed to be quite adequate.

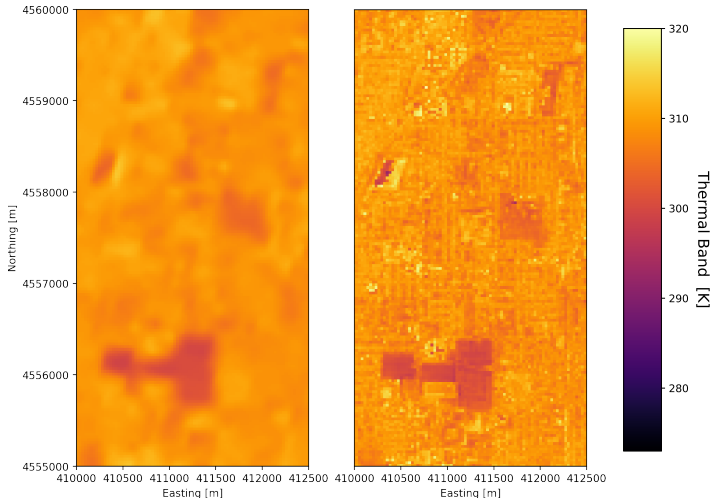

FIG. 3.5. Example plot of LS8 Band 10 interpolated by bicubic convolution (left) and the thermal bands sharpened by Gao et al. (2012) (right).

3.4 Image Processing

3.4.1 Initial Data Selection

Data were initially selected based on the quality of the Landsat 8 images. First, images that were lower than Tier-1 quality were removed. Then, only images with less than approximately 25% cloud cover over the study area were kept. Finally, if the ground observation data during the overpass was not considered to be good quality, the image for that day was not processed.

3.4.2 Masking criteria

Images were then masked using the CFMask quality assurance (QA) product created by USGS Earth Resources Observation and Science (EROS) center. This algorithm is used to detect possible clouds, cloud shadows, ice, water, terrain occlusions, and band saturation,

and stores the certainty of these features as bits in a per-pixel QA band. This product was used to mask out any features that weren't classified as "clear", and if the CFMask algorithm either (a) detected clouds over the golf course or (b) the algorithm failed to detect clouds, but the NDVI or Tir bands showed possible contamination over the golf course, the image was not used for analysis.

Land Cover and Impervious Surfaces

The triangle method operates under the assumption that the surfaces within the study area are either (a) fully vegetated, (b) bare soil, or (c) a combination of the two. In urban areas, pixel-scale land cover can also include buildings, roads, parking lots, or other impervious surfaces. Instead of either infiltrating into the soil, evaporating, or transpiring, a majority of the surface water runs off of these surfaces. However, it is very difficult to get a purely non-impervious pixel within an urban area, much less to get enough points to get the points to get a defined warm and cold edge.

In order to mask highly impervious surfaces, the impervious surface product from the National Land Cover Database (NLCD 2011) was used. The dataset's main purpose is to map various land covers at the Landsat 8 grid scale (Fig. 3.6), but it also provides a product that estimates the percentage of impervious surfaces for each pixel from 0-100%. After visually comparing a few different cutoffs for percent imperviousness, it was determined that 75% was the optimal balance between minimizing the lower protrusion in and possibly masking out pixels with vegetation. The areas masked out are shown in red in Fig. 3.7.

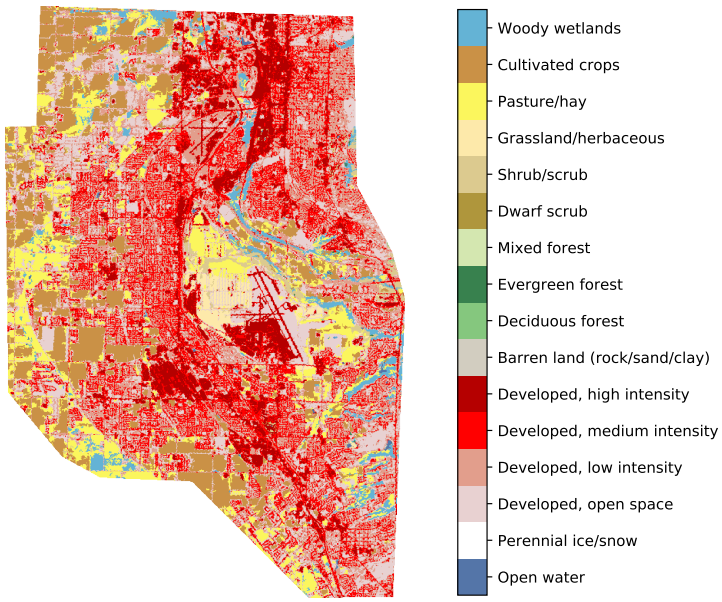

FIG. 3.6. Map of NLCD 2011 land classifications.

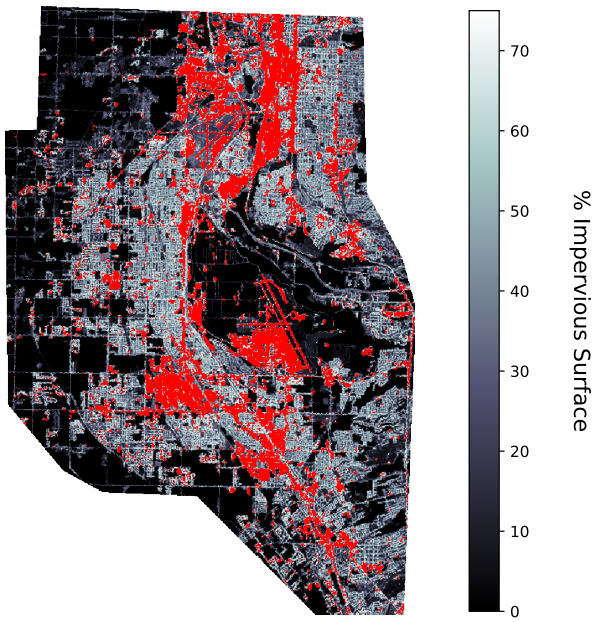

FIG. 3.7. Map of percent impervious surface per pixel, with values above 75% marked in red.

3.4.3 Triangle Method Calculation

One difficulty of the triangle method is the need for quantifying the cold and warm

edges, along with sensitivities to normalization. Attempts have been made to automate this process (Tang et al., 2010), but as urban surfaces are complex and usually masked for this model, the bounds were chosen visually. For normalization, maximum and minimum NDVI and T_{ir} (brightness temperature) values were set at the 99.5 and 0.5 quantiles, respectively, and were adjusted if there were anomalous pixels that were not masked out. Figure 3.8 shows the study area before and after normalization for a sample day.

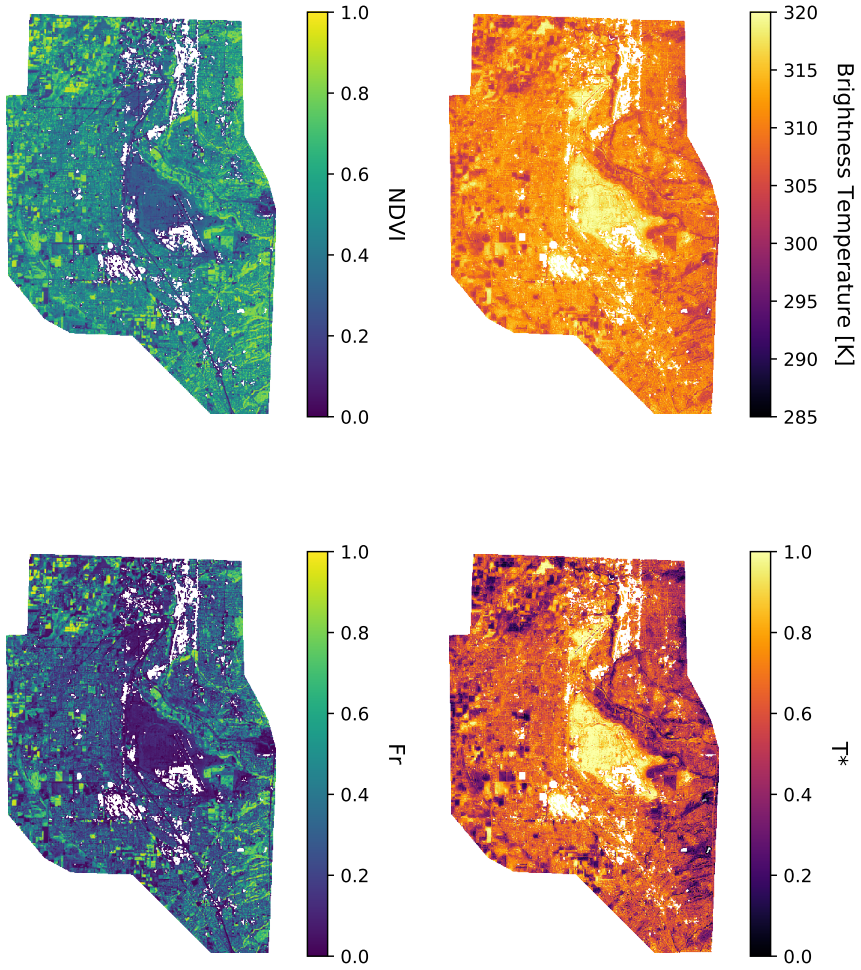

FIG. 3.8. NDVI and T_{ir} before and after being normalized for a Landsat 8 image on June 20th, 2017

The cold edge is defined by the locations of the lowest T_{ir} values at all NDVI values. In this case that led to an easy solution for a constant $T^* = 0$. The warm edge is generally a little more difficult to define precisely, especially in this case with surfaces that violate

the assumption that all points along the right side of the triangle should form a linear edge. The problem in an urban domain is the presence of dry pervious and impervious surfaces that have a large thermal inertia. The protrusion along the warm edge in Fig. 3.1 was not characterized by impervious surfaces. Rather, the pixels in this protrusion represent grass surfaces that were green when precipitation occurred during spring and autumn, but were not irrigated during the dry summer months. During dry periods, such surfaces can have large thermal inertia, that extends the temperature values outward in a "lobe". Due to the seasonality of this protrusion, there was not an attempt to mask these values out of the T_s-VI space. Rather, the resulting "lobe" was ignored in the placement of the warm edge during the summer months, as it would result in a warm edge that does not have the correct meaning. After all the bounds were chosen, evaporative fraction was calculated following Equations 3.4, 3.5, 3.6. A sample map of evaporative fraction is shown in Fig. 3.9.

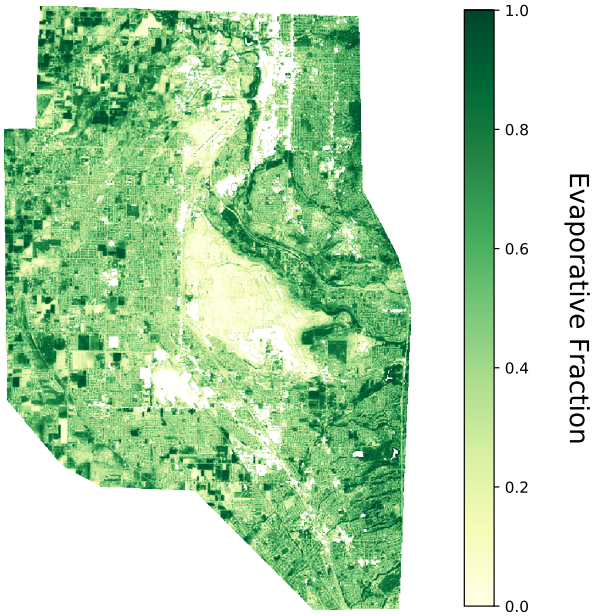

FIG. 3.9. Example evaporative fraction (EF) map for a Landsat 8 image on June 20th, 2017.

3.4.4 Footprint Model

One of the advantages of using eddy covariance measurements to help validate remote

sensing models of ET is the fact that these measurements represent an area upwind of the flux tower rather than a point measurement like a portable chamber or lysimeter. This means that the upwind area can be compared directly to pixels on the raster, rather than having to assume that one point measurement of ET is valid for the entire pixel area. To estimate how much of the upwind area is represented in the flux measurement, a flux footprint model was used. These models vary in complexity, ranging from relatively simple 1-D representations to complex 3-D inverse-Lagrangian models (Schmid, 2002). For this study, the model outlined in Kljun et al. (2015) was used, which is a parameterized version of an inverse-Lagrangian model which significantly reduces computation time. The model was run at a 3 m resolution using measurements from the flux tower. A sample footprint from the overpass on September 11th, 2018 is shown in Fig. 3.10. These footprints ensured that the calculated flux values came from the surface of interest (golf course), and allowed proper proper weighting of pixels in the triangle method EF model.

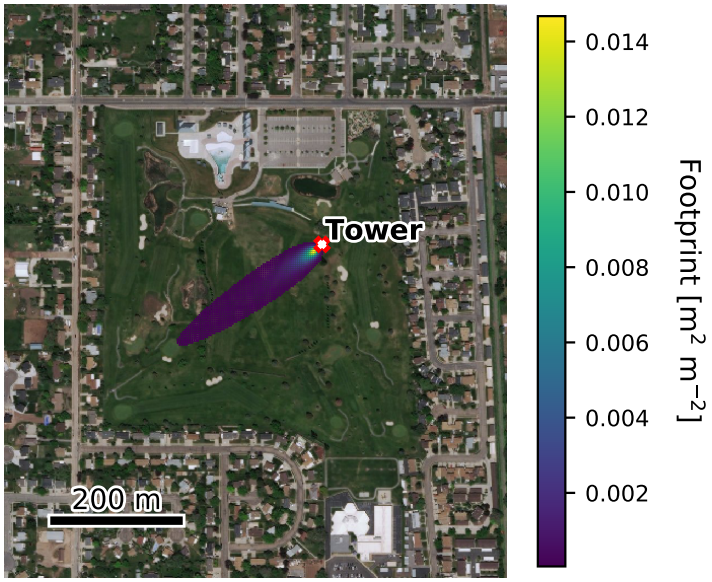

FIG. 3.10. Eagle Lake golf course study area, with example footprint from September 11th, 2018 containing 90% of the area contributing the flux. Sources: Esri, DigitalGlobe, GeoEye, i-cubed, USDA, USGS, AEX, Getmapping, Aerogrid, IGN, IGP, swisstopo, and the GIS User Community

3.5 Results and Discussion

3.5.1 NDVI and T_{ir} Timeseries

A few example points in different parts of the T_s-VI space were plotted as time series during the 2018 growing season in order to better understand how NDVI and T_{ir} change during the study period (Fig. 3.11). The three points chosen were the approximate location of the flux tower at the golf course (blue), a point in Hill Air Force Base (orange), and a suburban area west of Hill Air Force Base with medium density housing (red). The grey shaded areas on the plots were the normalization bounds used in Equations 3.2 and 3.3.

NDVI values for the suburban and golf course points ranged from 0.5 to 0.8, increasing towards the end of the season when there were lower temperatures and more frequent precipitation. The Hill AFB point had lower NDVI throughout the growing season, around 0.25, with a slight increase towards the end of the year. All of the points fell between the maximum and minimum NDVI bounds.

The trend in the thermal bands followed the typical summertime air temperature trend, with peak values occurring during July and August and decreasing during the fall months. The golf course had the coolest temperature for almost the entire growing season, the suburban point had slightly higher temperatures than the golf course, and Hill AFB had much higher temperatures for all dates other than near the end of the growing season, when all three points had similar temperatures.

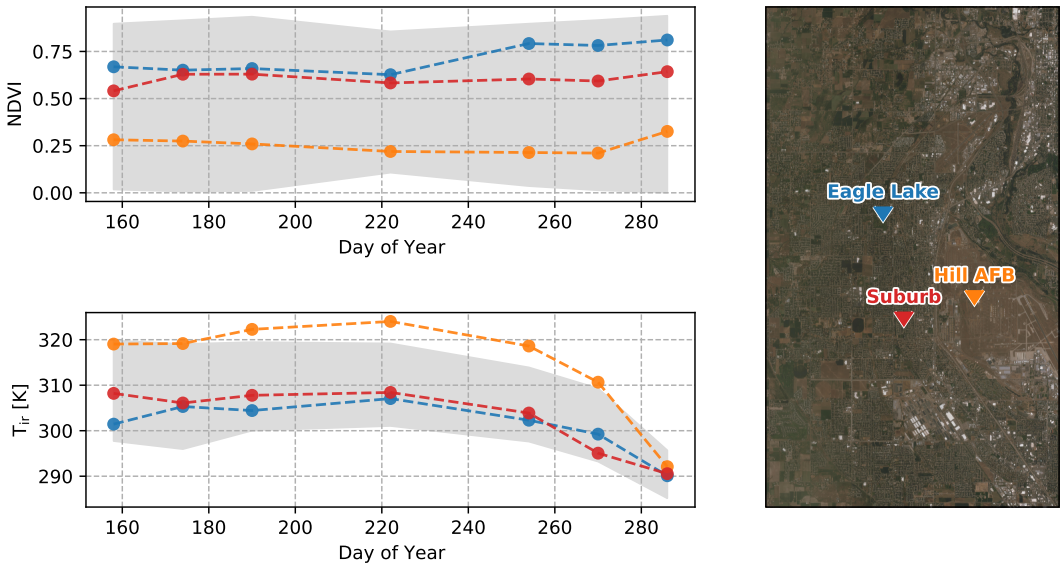

FIG. 3.11. (top and bottom) NDVI and T_{ir} values for three sample points during the 2018 growing season, with gray shading indicating the normalization values for NDVI and Tir. (right) Locations of the three points, with color markers matching the plots to the left.

3.5.2 Example Triangles

Two example triangles are shown here using the sharpened thermal bands obtained as described earlier. The first was from June 20th, 2017 (Fig. 3.12), represents the typical early- to mid-season triangle, with a somewhat trapezoidal shape that has a defined cold and highly vegetated vertex, and an expected "lobe" or protrusion along the lower-right hand side of the Ts-VI space (Fig. 3.12). The cold edge is not populated by a great many points as commonly observed and described in Carlson (2013) due to a lack of pixels with wet soil at lower fractional vegetation covers. In such cases the left most points actually define the cold edge. The protrusion of points in the lower right corner are due to surfaces with large thermal inertia as described earlier.

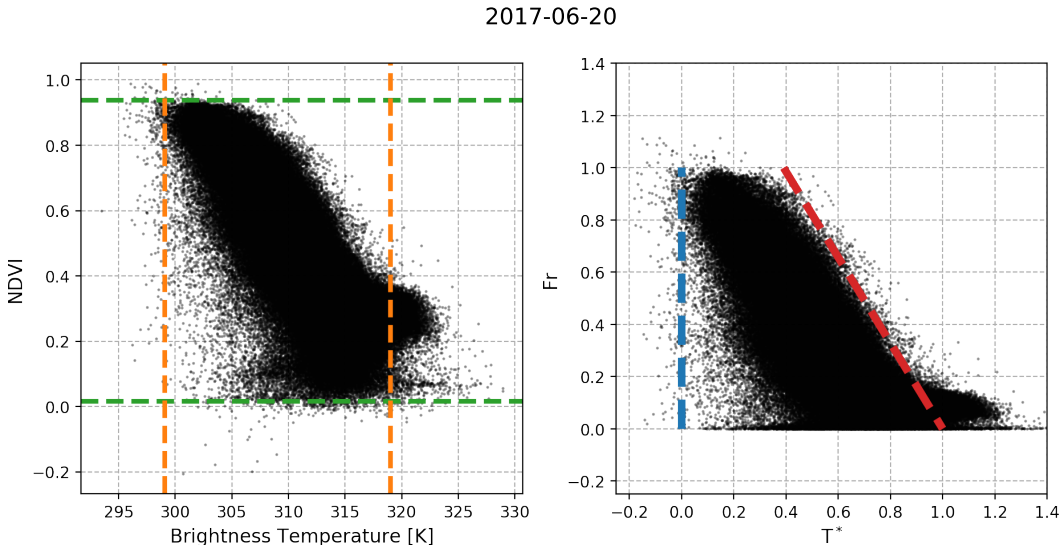

FIG. 3.12. Sample triangle from June 20th, 2017 that was typical of triangles during the early- to mid-season. (left) Triangle before normalization, with normalization values for NDVI shown in green and T_{ir} shown in orange. (right) Triangle after normalization, with the cold edge shown in blue and the warm edge shown in red.

The second triangle was from late in the growing season on October 13th, 2018 (Fig. 3.13). This represents how the typical triangle appears at the end of the growing season, with a poorly defined cold edge, a steep warm edge, and a somewhat rounded top at the highest fractional covers. The points at the cold edge were sparser than Fig. 3.12, and it was placed where the spatial density of the pixels rapidly changed at lower T_{ir} values. The warm edge placement was similar to Fig. 3.12, but the protrusion in the lower-right hand side of the T_s-VI space was much less pronounced. Therefore, the warm edge was placed where the density of pixels in this protrusion started to become less dense, rather than ignoring the protrusion entirely.

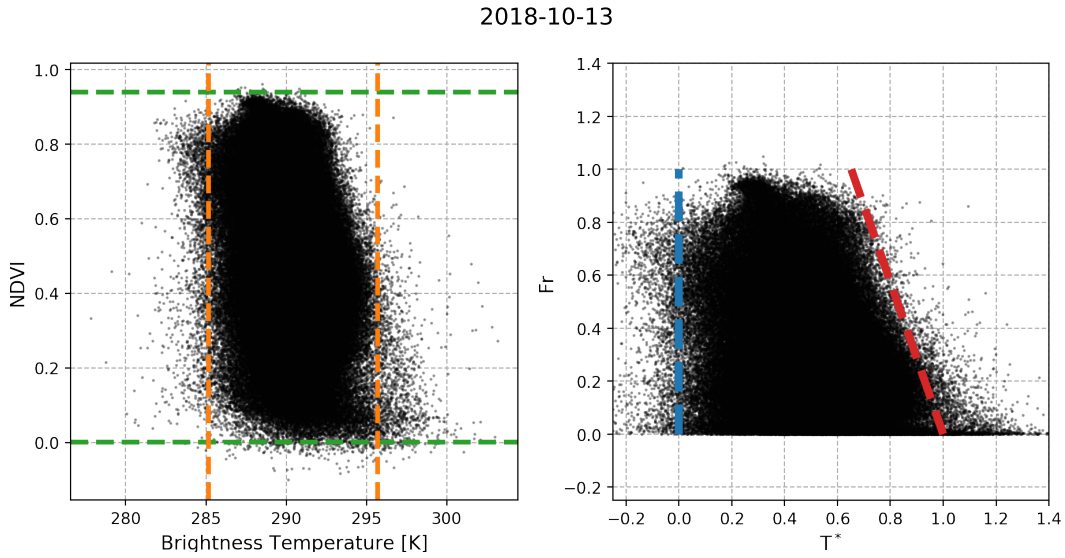

FIG. 3.13. Sample triangle from October 13th, 2018 that was typical of triangles during late-season. (left) Triangle before normalization, with normalization values for NDVI shown in green and T_{ir} shown in orange. (right) Triangle after normalization, with the cold edge shown in blue and the warm edge shown in red.

Triangles were also created using unsharpened thermal bands (100 m pixel size) that were interpolated to 30 m using the more common bicubic convolution, which was the thermal product included with the surface reflectance bands in GEE. Bounding values of NDVI were not changed because the same optical bands were used, but new T_{ir} bounds and warm edges were chosen using the same criteria as the sharpened bands. Normalization values, along with slope values for the warm edge, are shown in Tables 3.1 and 3.2.

One noticeable difference when using the unsharpened bands was that the range between the bounds changed, with $T_{ir,min}$ being 0.9 K cooler and $T_{ir,max}$ being 1.9 K warmer. The slopes of the warm edge also changed, and were steeper (on average) on the sharpened triangles. This change was most likely due to the sharpening algorithm, which was better able to catch the heterogeneity of surface temperatures for complex surfaces such as urban areas (see Fig. 3.5). Oftentimes there are roads, sidewalks, and buildings adjacent to vegetation, which are mixed together with 100 m pixel sizes. The interpolation scheme also caused much of the blurriness, as it integrated many surrounding pixels to reduce the number of artifacts, but in turn also smooths out individual features. This result underscores the importance of the quality of the thermal sharpening procedure on

the results, especially for a landscape with such significant spatial variability at many scales. Results from both the sharpened and unsharpened triangles are shown in the following section.

TABLE. 3.1. Triangle method inputs using the unsharpened thermal bands.

Date	**NDVI$_0$**	**NDVI$_s$**	**T$_{ir,min}$**	**T$_{ir,max}$**	**Warm Edge Slope**
2017-06-04	0.006	0.920	299.7	317.8	-2.309
2017-06-20	0.017	0.938	300.7	317.9	-2.227
2017-10-10	0.006	0.929	285.0	298.7	-2.294
2018-06-07	0.018	0.897	299.6	317.2	-2.058
2018-06-23	0.007	0.915	297.4	316.9	-2.045
2018-07-09	0.010	0.934	300.9	318.2	-2.392
2018-08-10	0.061	0.856	301.8	312.8	-2.058
2018-09-11	0.036	0.897	298.1	312.8	-2.037
2018-09-27	0.014	0.916	293.6	307.0	-2.058
2018-10-13	0.001	0.939	285.0	294.7	-7.246
mean	0.018	0.914	296.2	311.8	-2.672
s. dev.	0.018	0.025	6.3	8.7	1.612

TABLE. 3.2. Triangle method inputs using the sharpened thermal bands.

Date	**NDVI$_0$**	**NDVI$_s$**	**T$_{ir,min}$**	**T$_{ir,max}$**	**Warm Edge Slope**
2017-06-04	0.006	0.920	299.2	322.8	-1.520
2017-06-20	0.017	0.938	299.0	319.0	-1.642
2017-10-10	0.006	0.929	284.4	298.8	-2.146
2018-06-07	0.018	0.897	297.7	319.8	-1.443
2018-06-23	0.007	0.915	296.0	319.0	-1.381
2018-07-09	0.010	0.934	300.0	319.4	-1.433
2018-08-10	0.061	0.856	301.1	319.1	-1.323
2018-09-11	0.036	0.897	297.6	313.9	-1.429
2018-09-27	0.014	0.916	293.2	309.3	-1.486
2018-10-13	0.001	0.939	285.1	295.7	-2.874
mean	0.022	0.914	295.3	313.7	-1.668
s. dev.	0.031	0.025	6.0	9.4	0.483

3.5.3 Triangle Method Results

Figure 3.14 shows the EF measured at the flux tower compared to the EF calculated

using the triangle method using the sharpened thermal bands (orange) and unsharpened thermal bands (blue). The performance of the model was slightly better after sharpening for lower evaporative fractions, which often occurred during the end of the growing season, but root mean square error values were the same for both sets of thermal bands at 0.13. This is likely due to the large amounts of scatter at higher EF values, with the unsharpened bands actually performing better in this section. r^2 values for the 1:1 line were not reported as they were both negative, indicating that the mean station EF performs better than the model. The average values for the sharpened triangles was 0.79, 0.82 for the unsharpened triangles, and 0.84 for the station.

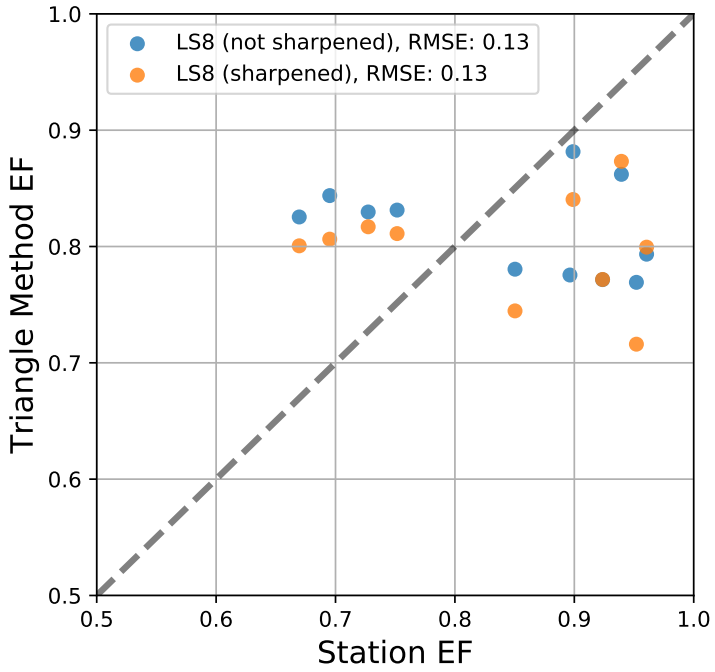

FIG. 3.14. Triangle method results for evaporative fraction. Colors indicate whether the thermal bands were sharpened or not.

However, when the station available energy ($R_n - G$) is used for both sets of data to get latent heat flux (LE) values, the agreement was much better, with the unsharpened and sharpened r^2 values going up to 0.82 and 0.81, respectively (Fig. 3.15). The root mean squared errors were also similar, with only 0.65 W m^{-2} separating the two. Still, the was a significant low bias at higher LE values, matching the trend in Fig. 3.14.

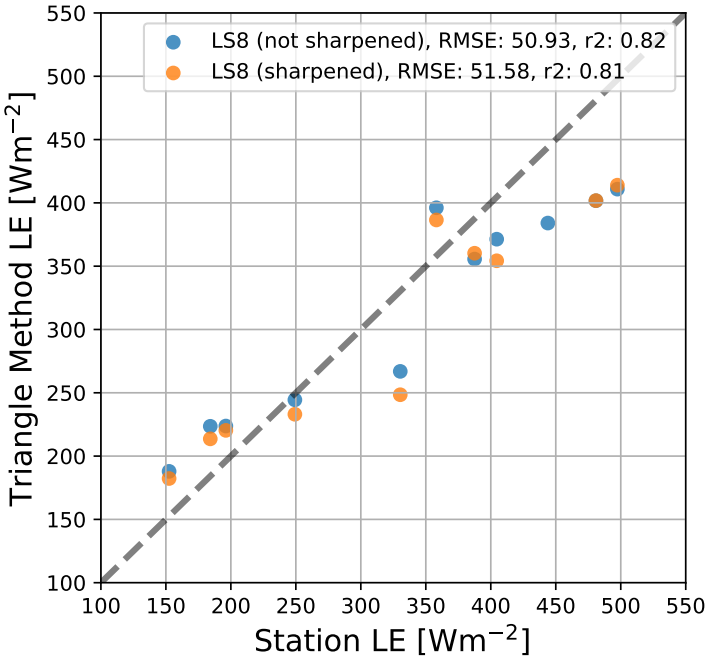

FIG. 3.15. Triangle method results for latent heat flux, using R_n and G from station. Colors indicate whether the thermal bands were sharpened or not.

3.5.4 NLCD Triangles

To better understand the performance of the triangle method in an urban area, more insight into how each land cover type changes the shape of the triangle is needed. While the example triangles in section 3.5.2 show how the T_s-VI space behaves for the urban area as a whole, it was also useful to see where different types of land cover fell within the T_s-VI space to see which land cover types contributed to different parts of the triangle. The NLCD 2011 dataset was used to classify each pixel with their respective land cover type, and was grouped with similar land types for each subplot in Fig. 3.16 (early- to mid-season) and Fig. 3.17 (late season).

Early- to Mid-Season NLCD Triangles

Urban landscapes (labeled "Developed" in the upper-left) were able to fill out most of the triangle in Fig. 3.16, with more built pixels having lower fractional covers. Normalized temperature did not have as clear of a relationship with built intensity, but there were some interesting features, notably the pockets of "open space" type pixels grouping along the top of the triangle and in the lower-right hand protrusion. This is likely due to the grouping

at the top of the triangle being irrigated, while the grouping in the protrusion being left fallow during the summer months.

Land cover types of forest, shrub and grassland, and wetlands all demonstrated a general trend of cooling with increasing fractional cover. Pasture and crops also followed this trend, although it filled out a larger portion of the triangle, forming a narrower but still trapezoidal shape. Cultivated crops were present for almost all fractional covers, and the pasture/hay classification filled out a large portion of the triangle as well, along with much of the protrusion. The pixels within the protrusion are in a similar location as the "developed, open area" pixels, which shows that these surfaces behave similarly at this time of year. These surfaces have larger thermal inertia, which distorts their locations in the triangle, as they are no longer governed by the same physics. This triangle underestimated the EF at the golf course, with the model having an EF of 0.80 while the station had an EF of 0.96.

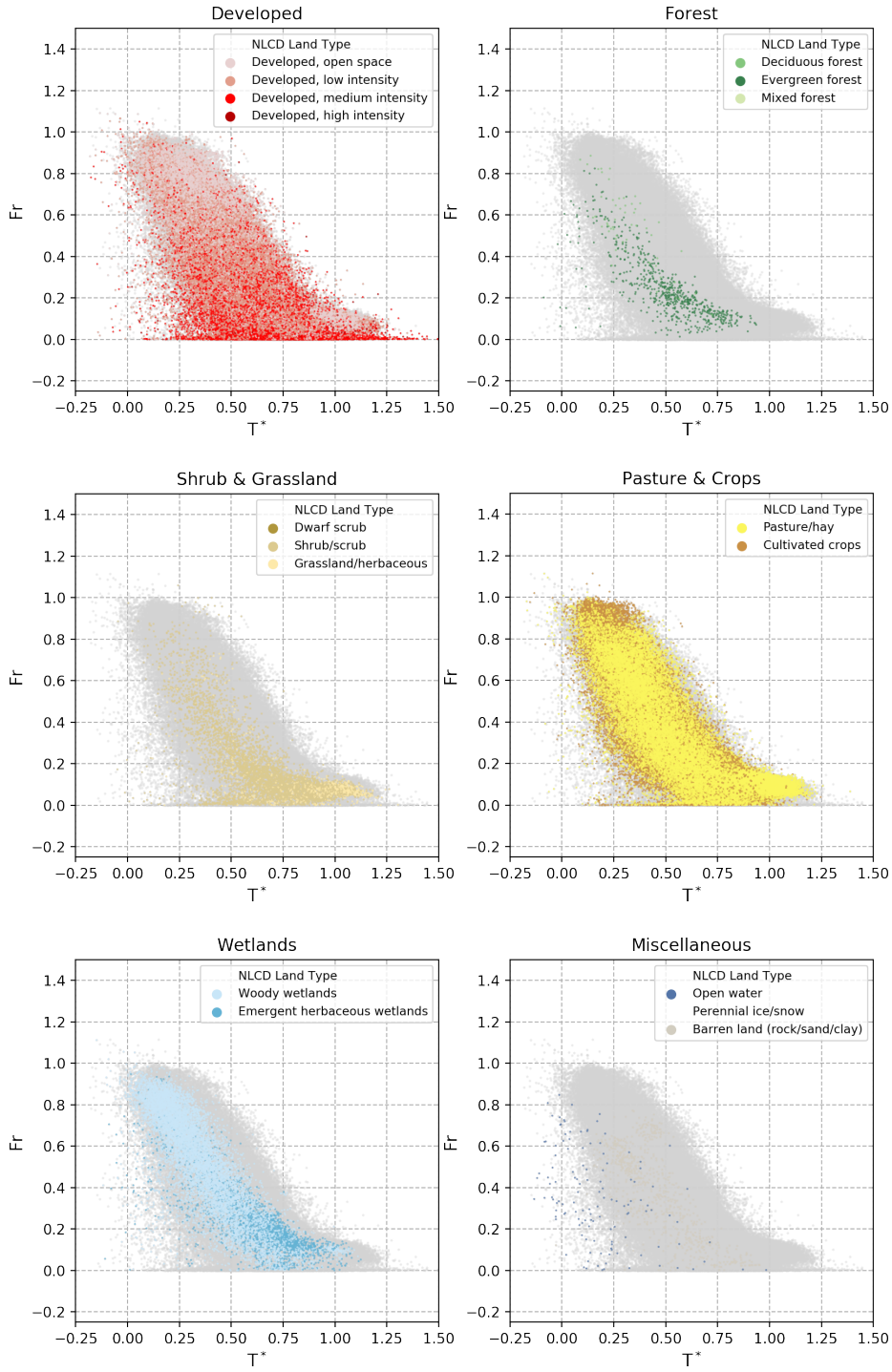

FIG. 3.16. NLCD 2011 land classification of each pixel in Fig. 3.12. The complete triangle is shown in gray on each subplot, and the colors indicate the land cover type listed in the legends.

Late-Season NLCD Triangles

Some of the same features as earlier in the season were observed at the end of the

season, such as cultivated crops appearing markedly at the top of the triangle in Fig. 3.17. But, later in the season, the sloping nature of many of the land cover types was less defined, with shrubland and grassland, forested, and emergent herbaceous wetlands all either having significantly less slope with more noise or losing the shape altogether. Woody wetlands, forests, and pasture/hay also had a large spread along the cold edge, which made the cold edge much more difficult to find.

One possible reason for this spread could be that the relationship between fractional cover and surface temperatures starts to fall apart near the end of the growing season as photosynthesis reduces and senescence of the vegetation occurs before the winter season. Cultivated crops still had a relatively well defined cold edge and better defined trapezoidal shape, so these surfaces could be used as a benchmark to create the cold edge. However, with little ET occurring and the model performing within the root mean square error (EF of 0.82 for the model and 0.73 observed), it may be worth putting more effort into improving warm (and possibly cold) edge placement for the summertime triangles.

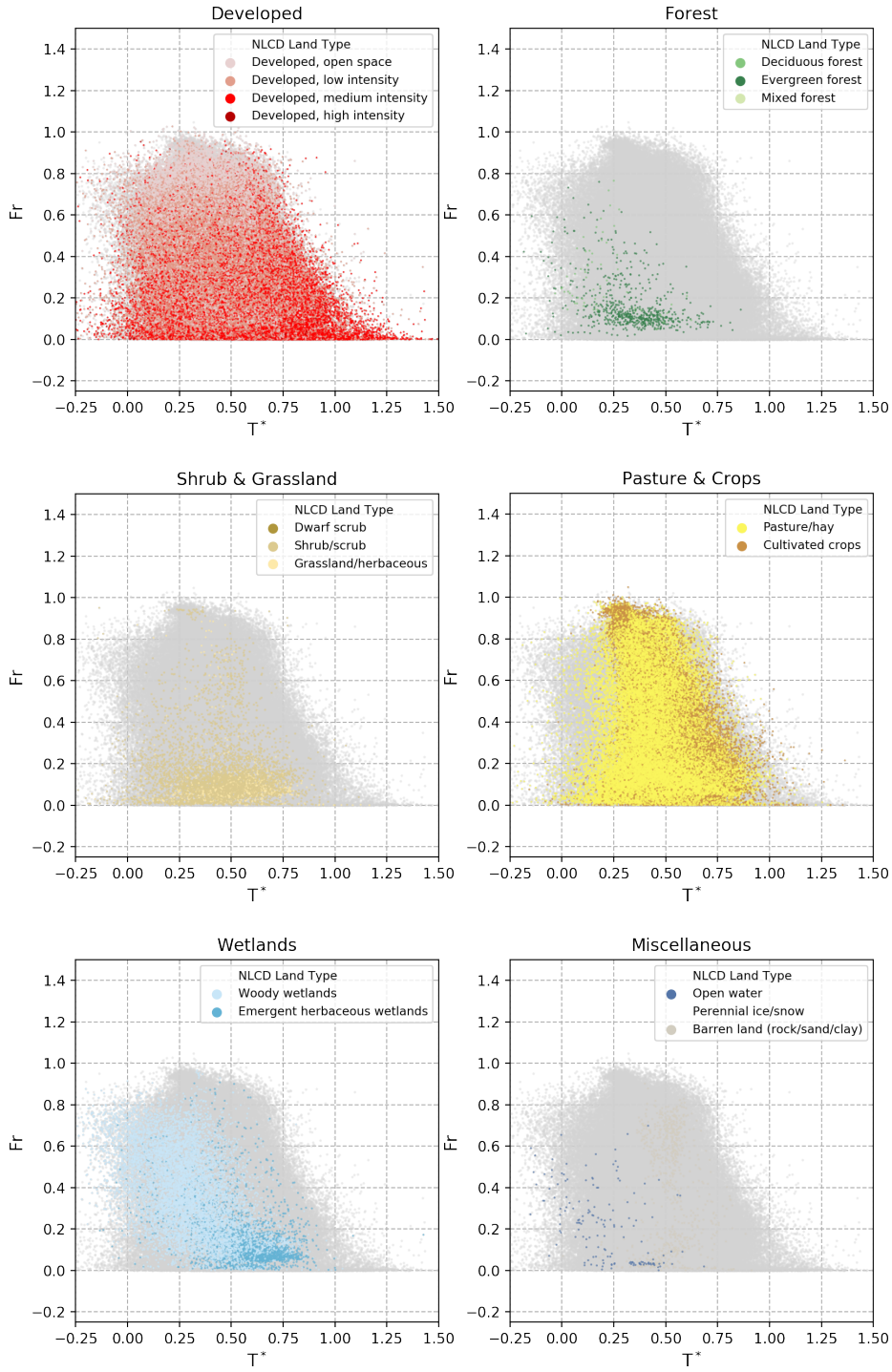

FIG. 3.17. NLCD 2011 land classification of each pixel in Fig. 3.13. The whole triangle is shown in gray on each subplot, and the colors indicate the land cover type listed in the legends.

3.6 Conclusions

Using remote sensing ET models in urban areas poses particular challenges, especially

for urban regions with a wide variety of land cover types. Here we tested a simple remote sensing model called the "triangle method", which uses normalized NDVI and brightness temperature, and the bounds that arise from plotting them against each other, to get evaporative fraction (EF).

After performing this analysis with Landsat 8 imagery during the 2017 and 2018 growing seasons and comparing them against observational values at an irrigated urban turfgrass site, it was found that while the model produced reasonable mean EF values (0.82 for unsharpened and 0.79 for sharpened vs. 0.84 for the station), there was lower correlation between modeled and observed values, and a root mean square error of 0.13. The model performance was in general worse than seen in other studies (e.g. de Tomás et al. (2014)), but showed results similar to Kim and Hogue (2013) for certain sites in semi-arid landscapes. The underperfomance of the model in this case may be due to a variety of factors, including surfaces with large thermal inertia such as roads and fallow ground, surfaces that dry out during the summer months, and pixels containing a large variety of surface types. When using station available energy for the model, modeled latent heat flux (LE) values compared well against the observed latent heat fluxes, but there was a significant low bias at higher LE values.

While the model does provide reasonable estimates of EF, there are many other challenges that need to be addressed before getting proper operational estimates of ET in urban areas. One of these challenges is the interpolation of extrapolating EF to daily scales. EF has been found to vary throughout the day (Crago, 1996), and is dependent on a variety of factors including cloud cover, heat advection from surrounding areas, and vegetation stress that are not addressed in the framework of the model. Other challenges such as lack of objectivity in choosing the warm and cold edges, surface heterogeneity within each pixel, and certain surfaces not following the trapezoidal shape also need to be addressed.

Further investigation needs to be done on a variety of urban surfaces to link their optical and thermal properties to remote sensing models at several spatial scales. Models based on the T_s-VI space may be able to estimate instantaneous variables such as EF, but are prone to the previously mentioned issues and do not explicitly model the components needed to

make daily ET measurements. Implementing urban landscapes into more complex models such as ALEXI/DisALEXI (Anderson et al., 2011) or METRIC (Allen et al., 2007) may prove to be a more fruitful endeavor as they are more equipped to deal with the complex interactions that occur between the urban surface and the atmosphere and can also produce estimates of urban ET that can be used by the public and decision makers.

CHAPTER 4

CONCLUSIONS

4.1 Summary of Results

4.1.1 Chapter 2

Eddy covariance measurements were made during the 2016-2018 growing seasons to quantify the ET of irrigated turfgrass and improve understanding of how ET is affected by environmental conditions. Daily energy balance closure values typically ranged from 0.69 to 0.95, but averaged 0.85 for a set of sample days, which is considered adequate when compared to those for other landscapes.

When looking at hourly closure values, there was a general increasing trend throughout the day. If the fetch during an hour was not optimal, median values were slightly lower than if the winds were from an optimal direction. Sample cospectra were also calculated from a certain subset of wind directions where there weren't significant obstructions, but thinly distributed trees were present upwind of the tower. It was found that these non-ideal fetches had an impact on the turbulent field, with the distribution of eddies shifting towards lower frequencies. It was decided that hours that had winds from this non-ideal fetch would not be used, but they may be useful for future analyses that change the averaging period or want to examine advection from the surrounding urban areas.

A sample day typical of a non-advective at the site was plotted alongside bulk stomatal and aerodynamic resistances to closer examine variables used in the Penman-Monteith equation. On these days latent heat flux was much higher than sensible heat flux, with vapor pressure deficit increasing throughout the day as temperature increased. While the aerodynamic resistance changed relatively little throughout the day, by the afternoon and early evening bulk stomatal resistance increased dramatically.

Hours that had winds from non-ideal fetches were gapfilled using an empirically derived hourly crop coefficients times reference ET calculated at the tower. Daily ET values of the

turfgrass using measured and gapfilled estimates ranged from 4 - 8 mm day^{-1} during the peak growing season, with the highest values occurring from June to early-July. These values then gradually decreased to 1-3 mm day^{-1} by the end of October. Measured values tended to be higher than the recommended daily ET (a crop coefficient of 0.8 times the reference ET) during the summer but were slightly lower than the recommended daily ET during most of the fall. Daily ET estimates were on the lower end compared to others in the literature that focused on only Kentucky Bluegrass (Romero and Dukes, 2016), but were comparable to a study with a similar climate and measurement method (Fenton, 2010), indicating that a dynamic crop coefficient may be useful for irrigation management at this and other sites in this region.

4.1.2 Chapter 3

Using remote sensing ET models in urban areas poses challenges, especially for urban areas with a wide variety of land cover types. Here, we tested a simple remote sensing model called the "triangle method" (Carlson, 2007). This method utilizes the relationship between satellite measurements of NDVI and brightness temperature for a large area to get evaporative fraction (EF).

Various processing steps were performed to attempt to account for the unique properties of the urban landscape. First the 90 m thermal bands of Landsat 8 were sharpened to 30 m using the algorithm in Gao et al. (2012) to better account for surface heterogeneity and the result was deemed adequate. Second any highly impervious surface was masked out, along with any other surface that did not conform to the model criteria such as ice, snow, water, etc. Finally, clouds were masked out using the most strict criteria in the CFMask QA product, and if any pixel in the study area was covered by clouds the whole image was discarded.

Then, after normalizing the T_s-VI space using percentiles of each distribution, the cold and warm bounds were determined. In general, the most arduous bound to determine was the warm edge, as a protrusion arose during the summer months that consisted of surfaces that were left fallow or unirrigated and showed signs of high thermal inertia. The shapes of

the triangles changed throughout the season as well, making it difficult to automatize the bound selection process.

After performing this analysis with Landsat 8 imagery during the 2017 and 2018 growing seasons and comparing them against observational values at an irrigated urban turfgrass site, it was found that while the model produced reasonable mean EF values (0.82 for unsharpened and 0.79 for sharpened vs. 0.84 for the station), there was a lack of significant correlation between modeled and observed values, and a root mean square error of 0.13. When using station available energy for the model, modeled latent heat flux (LE) values compared well against the observed latent heat fluxes, but there was a significant low bias at higher LE values.

To briefly investigate which surfaces contributed to which parts of the triangle, the National Land Cover Dataset (NLCD) for each pixel was plotted on a few example triangles. Landscapes that were considered to be "developed" filled most of the triangle, and various irrigated or naturally water-fed surfaces filled the left-hand side of the triangle. The protrusion consisted of "pasture/hay" and "developed, open area" land classifications, agreeing with the initial idea that the protrusion consisted of surfaces with high thermal inertia due to lack of irrigation. Multiple surfaces were found to temporally traverse the T_s-VI space from the summer to fall months, with the relationship between surface temperature and fractional cover becoming less defined.

4.2 Conclusions

As water concerns rise in the western United States, conspicuous water usage in populated areas (such as irrigation for large urban green spaces) can draw criticism from the public regardless of any social or ecological benefits. Therefore, it's important to understand exactly how much water these types of landscapes use in areas where irrigation is needed. Turfgrass is occasionally considered to be an "ideal" crop for irrigation management, as it is a relatively homogeneous crop that has water use that can, with some amount of uncertainty, can be irrigated using a relatively small amount of information. However, past studies, along with this thesis, have shown that this is usually not the case.

Eddy covariance and energy balance measurements were collected at a golf course subset in a suburban area in Roy, Utah, USA during the 2017 and 2018 growing season. Data in this thesis show that turfgrass can be a relatively large consumer of water when growing in a semi-arid region. Peak ET rates can range anywhere from 4-8 mm day^{-1} during optimal conditions. This can be anywhere from 1-2 mm day^{-1} higher than using the recommended crop coefficient (0.8) times reference evapotranspiration calculated using data at the site. There is a seasonal component to the difference as well, with actual ET becoming lower than the recommended watering rate by the end of the growing season. These seasonal changes need to be considered in order to irrigate urban landscapes such as golf courses if using methods involving reference evapotranspiration. Advection from the surrounding urban landscapes is also likely playing a role in the energy balance of the site, but more work needs to be done to quantify how much of a role it plays in the water use.

As satellite remote sensing platforms collect data that seemingly provide higher spatial, more wavebands, and/or higher temporal resolutions with each new platform, models using this data to provide estimates of ET are becoming more popular and robust. However urban areas are a daunting modeling problem as high spatial heterogeneity and building/landscape geometries are commonplace. This thesis explores one of the more simple approaches, the "triangle method" (Carlson, 2007), to compare observations of evaporative fraction (EF) at the golf course. There were some complications to using this approach, namely having many surfaces that violated the assumptions of the model during parts of the year despite attempts to mask such surfaces. Results were adequate when looking at only the means of the overpasses, but there was a lack of significant correlation between the station and modeled values. If one wants to continue fine-tuning this type of approach to estimate EF, exploring different masking strategies and placements of the "warm edge" would likely help improve performance.

Also, this thesis only compared a single observation of EF between the model and observations. To extrapolate this further, one must either assume that EF is constant throughout the day, which has been shown to not be the case at various sites, or to model how EF changes throughout the day. Estimates of net radiation and ground heat flux must also be made throughout the day to arrive at ET estimates, and these can be difficult to

estimate for heterogeneous urban landscapes due to advection from surrounding landscapes. More complex models such as ALEXI/DisALEXI (Anderson et al., 2011) or METRIC (Allen et al., 2007) may provide more physical frameworks to deal with urban landscapes, which can then be used to provide estimates of landscape ET that can be used by decision makers and the public.

REFERENCES

Allen, R. G., P. L. S, D. Raes, and S. Martin, 1998: Crop evapotranspiration-Guidelines for computing crop water requirements. *FAO Irrigation and drainage paper 56*.

Allen, R. G., and Coauthors, 2007: Satellite-Based Energy Balance for Mapping Evapotranspiration with Internalized Calibration (METRIC)—Applications. *Journal of Irrigation and Drainage Engineering*, **133 (4)**, 395–406, doi:10.1061/(ASCE)0733-9437(2007)133:4(395), 1509.06131.

Anderson, M. C., and Coauthors, 2011: Mapping daily evapotranspiration at field to continental scales using geostationary and polar orbiting satellite imagery. *Hydrology and Earth System Sciences*, **15 (1)**, 223–239, doi:10.5194/hess-15-223-2011, 1805.08172.

Aronson, L. J., A. J. Gold, and R. J. Hull, 1987: Cool-Season Turfgrass Responses to Drought Stress. *Wiley Online Library*, **27 (6)**, 1261–1266.

Barnett, T. P., and Coauthors, 2008: Human-Induced Changes in the Hydrology of the Western United States. *Science*, **319 (February)**, 1080–1083, doi:10.1126/science.1152538.

Bijoor, N. S., D. E. Pataki, D. Haver, and J. S. Famiglietti, 2014: A comparative study of the water budgets of lawns under three management scenarios. *Urban Ecosystems*, **17**, 1095–1117, doi:10.1007/s11252-014-0361-4.

Bonafoni, S., R. Anniballe, B. Gioli, and P. Toscano, 2016: Downscaling landsat land surface temperature over the urban area of Florence. *European Journal of Remote Sensing*, **49**, 553–569, doi:10.5721/EuJRS20164929.

Brown, P. W., C. F. Mancino, M. H. Young, T. L. Thompson, P. J. Wierenga, and D. M. Kopec, 2001: Penman Monteith Crop Coefficients for Use with Desert Turf Systems. *Crop Science*, **41 (1992)**, 1197–1206, doi:10.2135/cropsci2001.4141197x.

Brutsaert, W., 1975: On a derivable formula for long-wave radiation from clear skies. *Water Resources Research*, **11 (5)**, 742–744, doi:10.1029/WR011i005p00742.

Brutsaert, W., 1982: Evaporation into the atmosphere: Theory. *History, and Applications*, **1**.

Carlson, T., 2007: An overview of the "triangle method" for estimating surface evapotranspiration and soil moisture from satellite imagery. *Sensors*, **7 (8)**, 1612–1629, doi:10.3390/s7081612.

Carlson, T. N., 2013: Triangle models and misconceptions. *International Journal of Remote Sensing Applications*, **3 (3)**, 155–158.

Carlson, T. N., and D. A. Ripley, 1997: On the relation between NDVI, fractional vegetation cover, and leaf area index. *Remote Sensing of Environment*, **62 (3)**, 241–252, doi:10.1016/S0034-4257(97)00104-1.

Chávez, J., C. M. U. Neale, L. E. Hipps, J. H. Prueger, and W. P. Kustas, 2005: Comparing Aircraft-Based Remotely Sensed Energy Balance Fluxes with Eddy Covariance Tower Data Using Heat Flux Source Area Functions. *Journal of Hydrometeorology*, **6 (6)**, 923–940, doi:10.1175/jhm467.1.

Costello, L. R., and K. S. Jones, 2014: WUCOLS IV: Water Use Classification of Landscape Species. California Center for Urban Horticulture. University of California, Agriculture and Natural Resources.

Crago, R. D., 1996: Conservation and variability of the evaporative fraction during the daytime. *Journal of Hydrology*, **180 (1-4)**, 173–194, doi:10.1016/0022-1694(95)02903-6.

de Tomás, A., H. Nieto, R. Guzinski, J. Salas, I. Sandholt, and P. Berliner, 2014: Validation and scale dependencies of the triangle method for the evaporative fraction estimation over heterogeneous areas. *Remote Sensing of Environment*, **152**, 493–511, doi:10.1016/j.rse.2014.06.028.

Dieter, C. A., M. A. Maupin, R. R. Caldwell, M. A. Harris, T. I. Ivahnenko, J. K. Lovelace, N. L. Barber, and K. S. Linsey, 2018: Estimated use of water in the United States in 2015 - Circular 1441. Tech. rep., U.S. Geological Survey, 1–76 pp. doi:10.3133/cir1441.

Feigenwinter, C., R. Vogt, and A. Christen, 2012: *Eddy Covariance Measurements Over Urban Areas*. Springer, doi:10.1007/978-94-007-2351-1.

Feldhake, C. M., R. E. Danielson, and J. D. Butler, 1983: Turfgrass Evapotranspiration. I. Factors Influencing Rate in Urban Environments. *AGRONOMY JOURNAL*, **75**, 7.

Fenton, L. L., 2010: Evapotranspiraiton of Kentucky Bluegrass. M.S. thesis, Utah State University.

Foken, T., 2008: Eddy Flux Measurements the Energy Balance Closure Problem : An Overview. *Ecol. Appl.*, **18 (September)**, 1351–1367, doi:10.1890/06-0922.1.

Gao, F., W. P. Kustas, and M. C. Anderson, 2012: A data mining approach for sharpening thermal satellite imagery over land. *Remote Sensing*, **4 (11)**, 3287–3319, doi:10.3390/rs4113287.

Gillies, R. R., and T. N. Carlson, 1995: Thermal Remote Sensing of Surface Soil Water Content with Partial Vegetation Cover for Incorporation into Climate Models. *Journal of Applied Meteorology*, 745–756, doi:10.1175/1520-0450(1995)034<0745:TRSOSS>2.0.CO;2.

Green, R., J. Beard, and D. Casnoff, 1990: Leaf Blade Stomatal Characterizations and Evapotranspiration Rates of 12 Cool-season Perennial Grasses. *HortScience*, **25 (7)**, 760–761, doi:10.21273/HORTSCI.25.7.760.

Grimmond, C. S. B., and T. R. Oke, 1999: Evapotranspiration rates in urban areas. *Impacts of Urban Growth on Surface Water and Groundwater Quality*, **259**, 235–243, doi:10.1371/journal.pone.0124899.

Harivandi, M. A., J. Baird, J. Hartin, M. Henry, and D. Shaw, 2009: *Managing Turfgrasses during Drought*. University of California, Agriculture and Natural Resources, doi:10.3733/ucanr.8395.

Huang, B., and J. D. Fry, 2000: Turfgrass Evapotranspiration. *Journal of Crop Production*, **2 (2)**, 317–333, doi:10.1300/J144v02n02_14.

Jia, X., M. D. Dukes, and J. M. Jacobs, 2009: Bahiagrass crop coefficients from eddy correlation measurements in central Florida. *Irrigation Science*, **28 (1)**, 5–15, doi:10.1007/s00271-009-0176-x.

Jiang, L., and S. Islam, 2001: Estimation of surface evaporation map over southern Great Plains using remote sensing data. *Water Resources Research*, **37 (2)**, 329–340, doi:10.1029/2000WR900255.

Johnson, T. D., and K. Belitz, 2012: A remote sensing approach for estimating the location and rate of urban irrigation in semi-arid climates. *Journal of Hydrology*, **414-415**, 86–98, doi:10.1016/j.jhydrol.2011.10.016.

Kim, J., and T. S. Hogue, 2013: Evaluation of a MODIS triangle-based evapotranspiration algorithm for semi-arid regions. *Journal of Applied Remote Sensing*, **7 (1)**, 073 493, doi:10.1117/1.JRS.7.073493.

Kljun, N., P. Calanca, M. W. Rotach, and H. P. Schmid, 2015: A simple two-dimensional parameterisation for Flux Footprint Prediction (FFP). *Geoscientific Model Development*, **8 (11)**, 3695–3713, doi:10.5194/gmd-8-3695-2015.

Kotthaus, S., and C. S. Grimmond, 2012: Identification of Micro-scale Anthropogenic CO2, heat and moisture sources - Processing eddy covariance fluxes for a dense urban environment. *Atmospheric Environment*, **57**, 301–316, doi:10.1016/j.atmosenv.2012.04.024.

Leksungnoen, N., P. G. Johnson, and R. K. Kjelgren, 2012: Physiological responses of turfgrass species to drought stress under high desert conditions. *HortScience*, **47 (1)**, 105–111.

Massman, W. J., 2000: A simple method for estimating frequency response corrections for eddy covariance systems. *Agricultural and Forest Meteorology*, **104 (3)**, 185–198, doi:10.1016/S0168-1923(00)00164-7.

Monteith, J. L., 1965: Evaporation and environment. *Symposia of the society for experimental biology*, Cambridge University Press (CUP) Cambridge, Vol. 19, 205–234.

Nouri, H., S. Beecham, F. Kazemi, and A. M. Hassanli, 2013: A review of ET measurement techniques for estimating the water requirements of urban landscape vegetation. *Urban Water Journal*, **10 (4)**, 247–259, doi:10.1080/1573062X.2012.726360.

Perlich, P. S., M. Hollingshaus, E. R. Harris, J. Tennert, and M. T. Hogue, 2017: Utah's Long-Term Demographic and Economic Projections Summary. Tech. Rep. July, University of Utah, 32 pp.

Petropoulos, G., T. N. Carlson, M. J. Wooster, and S. Islam, 2009: A review of Ts/VI remote sensing based methods for the retrieval of land surface energy fluxes and soil surface moisture. *Progress in Physical Geography*, **33 (2)**, 224–250, doi:10.1177/0309133309338997.

Price, J. C., 1990: Using Spatial Context in Satellite Data to Infer Regional Scale Evapotranspiration. *IEEE Transactions on Geoscience and Remote Sensing*, **28 (5)**, 940–948, doi:10.1109/36.58983.

Roberts, E. C., W. W. Huffine, F. V. Grau, and J. J. Murray, 1992: Turfgrass Science-Historical Overview. *Agronomy Monographs*, D. V. Waddington, R. N. Carrow, and R. C. Shearman, Eds., American Society of Agronomy, Crop Science Society of America, Soil Science Society of America, Madison, WI, USA, 1–27, doi:10.2134/agronmonogr32.c1.

Romero, C. C., and M. D. Dukes, 2016: Review of Turfgrass Evapotranspiration and Crop Coefficients. *Transactions of the ASABE*, **59 (1)**, 207–223, doi:10.13031/trans.59.11180.

Schmid, H. P., 2002: Footprint modeling for vegetation atmosphere exchange studies: A review and perspective. *Agricultural and Forest Meteorology*, **113 (1-4)**, 159–183, doi:10.1016/S0168-1923(02)00107-7.

Spronken-Smith, R. A., T. R. Oke, and W. P. Lowry, 2000: Advection and the Surface Energy Balance Across an irrigated urban park. *International Journal of Climatology*, **20 (July)**, 1033–1047, doi:10.1002/1097-0088(200007)20.

Starkenburg, D., S. Metzger, G. J. Fochesatto, J. G. Alfieri, R. Gens, A. Prakash, and J. Cristóbal, 2016: Assessment of despiking methods for turbulence data in micrometeorology. *Journal of Atmospheric and Oceanic Technology*, **33 (9)**, 2001–2013, doi:10.1175/JTECH-D-15-0154.1.

Tang, R., Z. L. Li, and B. Tang, 2010: An application of the Ts-VI triangle method with enhanced edges determination for evapotranspiration estimation from MODIS data in arid and semi-arid regions: Implementation and validation. *Remote Sensing of Environment*, **114 (3)**, 540–551, doi:10.1016/j.rse.2009.10.012.

Twine, T. E., and Coauthors, 2000: Correcting eddy-covariance flux underestimates over a grassland. *Agricultural and Forest Meteorology*, **103 (3)**, 279–300, doi:10.1016/S0168-1923(00)00123-4.

Wang, C., J. Yang, S. W. Myint, Z. H. Wang, and B. Tong, 2016: Empirical modeling and spatio-temporal patterns of urban evapotranspiration for the Phoenix metropolitan area, Arizona. *GIScience and Remote Sensing*, **53 (6)**, 778–792, doi:10.1080/15481603.2016.1243399.

Webb, E. K., G. I. Pearman, and R. Leuning, 1980: Correction of flux measurements for density effects due to heat and water vapour transfer. *Quarterly Journal of the Royal Meteorological Society*, **106 (447)**, 85–100, doi:10.1002/qj.49710644707.

Wilson, K., and Coauthors, 2002: Energy balance closure at FLUXNET sites. *Agricultural and Forest Meteorology*, **113 (1-4)**, 223–243, doi:10.1016/S0168-1923(02)00109-0.

Yoon, J. H., S. Y. Wang, R. R. Gillies, B. Kravitz, L. Hipps, and P. J. Rasch, 2015: Increasing water cycle extremes in California and in relation to ENSO cycle under global warming. *Nature Communications*, **6**, 1–6, doi:10.1038/ncomms9657.

APPENDIX

A.1 Data Corrections

NR-Lite2

There were multiple changes in the instrumentation that measured net radiation during the 2017 and 2018 growing seasons. The first change occurred at the beginning of the 2017 growing season when a SN-500 4-way net radiometer (Apogee Instruments Inc., Logan, UT, USA) was installed alongside a 2-way NR-Lite2 net radiometer (Kipp & Zonen, Delft, The Netherlands). These two instruments ran in parallel for the 2017 growing season to obtain a relationship between the net radiation readings, given the SN-500 would be considered the standard.

All daytime data was used to obtain this linear fit. However, any net radiation values below zero W m^{-2} on either instrument were not used due to fundamental differences between how the 2-component NR-Lite2 and the 4-component SN-500 measure net radiation. The resulting relationship is shown in Figure A.1. With an r^2 value of 0.98 and a root mean squared difference of 25.27 W m^{-2} over all positive net radiation values, it was decided that the linear relationship of $R_{n,corr} = 1.05R_{n,raw} + 17.2$ was an appropriate correction to the raw data. The NR-lite2 was then decommissioned at the end of the season.

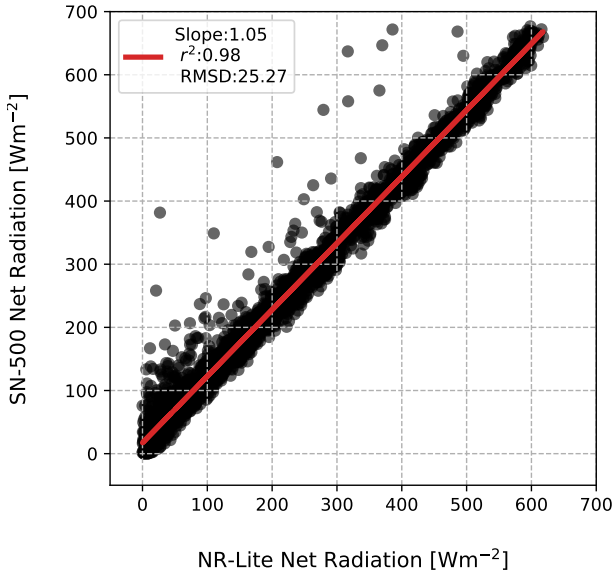

FIG. A.1. Comparison of net radiation values from the SN-500 vs. NR-Lite2 during the 2017 growing season. The linear relationship between the two instruments is shown in red, which had a y-intercept of 17.2 W m^{-2}.

A.2 Soil Bulk Density Samples

Soil bulk density samples were obtained around the flux tower, as they are needed to determine energy storage in the layer of soil above the heat flux plates. These samples were taken by removing soil cores in both good quality turf and medium to poor quality turf on October 23rd, 2018. Once these samples were obtained, they were placed into pre-weighed bags and were then weighed again before being dried in an oven for 24 hours to remove all of the water from the soil. The dry soil was then weighed one more time to get the weight of the water evaporated from the soil. Bulk density was then calculated using the following equation:

$$\rho_v = \frac{m_{soil,dry}}{sample\ volume} \tag{A.1}$$

where $m_{soil,dry}$ (g) was the mass of dry soil and *sample volume* was the volume of the soil sample cm^3. The gravimetric water content was also calculated for these samples:

$$\theta_g = \frac{m_{water}}{m_{soil}} = \frac{m_{soil,wet} - m_{soil,dry}}{m_{soil,dry}} \tag{A.2}$$

where $m_{soil,wet}$ (g) was the mass of the soil sample before drying. The values are shown in Table A.1, and a bulk density of 1.3 g cm^{-3} was used when estimating ground heat flux.

TABLE. A.1. Bulk density samples taken around the weather station. Samples are split up into soil below uniform turf (good quality) and patchy turf (medium to poor quality). All samples were collected on October 23rd, 2018.

Depth cm	**Bulk Density** $g\,cm^{-3}$	**Gravimetric Water Content** $g\,g^{-1}$
Uniform Turf		
8.3	1.40	0.24
6.0	1.31	0.28
Patchy Turf		
8.4	1.33	0.21
6.0	1.21	0.23